Edgars Edelmers

ORCID 0000-0001-5329-4426

Automated Morphological Structure Detection, Segmentation, and 3D Model Reconstruction from Medical Images Using Artificial Intelligence Deep Neural Network Technologies

Summary of the Doctoral Thesis for obtaining the scientific degree "Doctor of Science (*PhD*)"

Sector Group – Medical and Health Sciences

Sector – Basic Medicine

Sub-Sector – Anatomy

Riga, 2025

The Doctoral Thesis was developed at Rīga Stradiņš University

Supervisors of the Doctoral Thesis:

Dr. med., Associate Professor **Dzintra Kažoka**,
Rīga Stradiņš University, Latvia

Dr. sc. ing., Associate Professor **Katrīna Šmite**,
Riga Technical University, Latvia

Scientific Advisors:

Dr. med., Associate Professor **Maija Radziņa**,
University of Latvia

Dr. sc. comp., Leading Researcher **Kaspars Sudars**,
Institute of Electronics and Computer Science, Latvia

Official Reviewers:

Dr. habil. med., Professor **Jānis Vētra**,
Rīga Stradiņš University, Latvia

Dr. sc. ing., Professor **Jānis Ločs**,
Baltic Biomaterials Centre of Excellence (BBCE), Latvia

PhD, Professor **Darius Batulevičius**,
Lithuanian University of Health Sciences

Defence of the Doctoral Thesis will take place at the public session of the Promotion Council of Basic Medicine on 29 December 2025 at 10.00 in the Hippocrates Lecture Theatre, 16 Dzirciema Street, Rīgas Stradiņš University

The Doctoral Thesis is available in RSU Library and on RSU website:
https://www.rsu.lv/en/dissertations

Secretary of the Promotion Council:

Dr. habil. med., Professor **Valērija Groma**

Table of Contents

Abbreviations

AI	Artificial Intelligence
ANO1	Anoctamin-1 (calcium-activated chloride channel)
CPU	Central Processing Unit
CT	Computed Tomography
DICOM	Digital Imaging and Communications in Medicine
DSC	Dice Similarity Coefficient
FDM	Fused Deposition Modelling
FFPE	Formalin-Fixed, Paraffin-Embedded (tissue)
FOV	Field of View
ICC	Interstitial Cells of Cajal
IoU	Intersection-over-Union
mAP	mean Average Precision
mAP50	mAP at IoU = 0.50
mAP50-95	mAP averaged over IoU = 0.50 – 0.95
MRT	Magnetic Resonance Tomography
NIfTI	Neuroimaging Informatics Technology Initiative file format
nnU-Net	“no-new-U-Net” U-Net framework
NRRD	Nearly Raw Raster Data file format
OBJ	Wavefront Object file format
PD-L1	Programmed Death-Ligand 1
PLA	Polylactic Acid (bioplastic filament)
PVA	Polyvinyl Alcohol (water-soluble support material)
ROI	Region of Interest
RSU	Rīga Stradiņš University
STL	Stereolithography file format
U-Net	“U” shaped convolutional network for image segmentation
WSI	Whole-Slide Image
YOLO-v11	You Only Look Once, version 11 (object-detection network)
µCT	Micro Computed Tomography

Introduction

Modern medicine and biology rely heavily on imaging to understand the human body, from large anatomical structures down to the cellular level. Radiological scans like computed tomography (CT) and magnetic resonance tomography (MRT) provide detailed three-dimensional views of organs and tissues. In parallel, digital histology reveals the microscopic world of cells. A common challenge across all these modalities is the sheer volume and complexity of the data, which makes manual analysis time-consuming and subject to variation between experts. To address this, two key technologies offer powerful solutions: artificial intelligence (AI) can automate image analysis with remarkable speed and precision, while 3D printing can transform digital scans into tangible anatomical models. However, these advanced fields often operate independently. This Thesis investigates how to build a unified and reliable workflow that connects them, using AI to automatically analyse medical images at both the anatomical and cellular scales to create accurate 3D models and quantitative reports for education and clinical practice.

Aim of the Thesis

This study aims to develop and validate an artificial intelligence (AI) based methodology that uses deep neural networks for automated detection and segmentation of morphological structures in medical images, as well as to design a protocol to reconstruct three-dimensional (3D) anatomical models from segmented medical imaging data.

Objectives of the Thesis

The following objectives are set to achieve the aim of the Doctoral Thesis:

1 Develop a reproducible protocol to reconstruct anatomically accurate 3D bone models from various medical imaging sources (including CT, µCT, photogrammetry, 3D scanning).

2 Validate the reconstructed bone anatomical models by fabricating them with fused deposition modelling (3D printing).

3 Assemble annotated datasets of segmented morphological structures at two scales, comprising vertebrae with lytic and sclerotic lesions from computed tomography as well as intestinal Cajal cells from immunohistochemically stained histological whole slide images.

4 Train a deep neural network models for the automatic detection and segmentation of these morphological structures.

5 Create and validate the methodologies by implementing them in software for automatic detection and segmentation of morphological structures.

Hypothesis of the Thesis

Advanced image processing techniques, including those utilising deep neural network architectures, can provide reliable and reproducible results in the detection and segmentation of morphological structures with sufficient level of accuracy for both medical diagnostic applications and the reconstruction of anatomical 3D models.

Novelty of the Thesis

Prior to the research conducted in this Doctoral Thesis, the field of medical image analysis had advanced significantly beyond simple manual delineation, yet substantial barriers remained that prevented the seamless integration of these technologies into clinical and educational workflows. The primary challenges in the field had shifted from questions of technical feasibility to issues of scalability, data efficiency, and precision, particularly when dealing with complex pathologies and histological structures.

One of the most significant hurdles was the "Annotation Bottleneck" inherent in modern Deep Learning. While convolutional neural networks, such as the U-Net and V-Net architectures, established a new baseline for medical image segmentation, they introduced a critical dependency on massive, high-quality labelled datasets (Milletari et al., 2016; Ronneberger et al., 2015). Creating these "ground truth" datasets remained a manual, labour-intensive process, often stalling artificial intelligence implementation due to the sheer cost of expert time required to annotate thousands of training examples. Although interactive algorithms like "Graph Cuts" and "Random Walker" were adopted to alleviate this burden, they typically relied on intensity gradients and struggled with the "weak boundaries" common in soft tissues and spinal structures, often requiring substantial user correction that negated their efficiency gains (Boykov & Jolly, 2001; Grady, 2006).

A parallel challenge existed in the domain of digital pathology, specifically regarding the quantification of morphological structures in whole slide images. The quantification of specific cell types, such as interstitial cells of Cajal, was predominantly manual or semi-automated using morphological filters, frequently implemented in legacy commercial image-analysis environments, where user-defined macros and threshold-based routines were tailored for each staining protocol and then laboriously tuned and validated. Standard object detection models utilising horizontal bounding boxes also proved inadequate for these tasks. As noted by Ma et al., when such models are applied to elongated, spindle-shaped cells like interstitial cells of Cajal, they capture excessive background and often suppress adjacent diagonal cells due to high intersection over union overlap, leading to systematic undercounting in dense tissue clusters (Ma et al., 2018). More recent digital pathology ecosystems, including Visiopharm, Definiens Tissue Studio, Image-Pro (Media Cybernetics), Indica Labs' HALO,

and the Aperio HALO AP platform, provide integrated workflows for whole-slide tissue segmentation and immunohistochemistry scoring, and are now widely used in translational research, clinical trials, and biomarker studies (Escobar Díaz Guerrero et al., 2022; Salo et al., 2024). However, these systems remain proprietary "black boxes": algorithmic details and model parameters are generally inaccessible to end-users, and workflow customisation is constrained by vendor-specific interfaces. In addition, substantial licensing and maintenance costs limit their deployment in many academic and educational settings, despite the availability of open-source alternatives such as Orbit and QuPath, which have demonstrated robust performance for whole-slide image analysis and biomarker quantification but often require considerable technical expertise in scripting, workflow configuration, and computational infrastructure, thereby posing additional barriers for laboratories without dedicated informatics support (Bankhead et al., 2017; Stritt et al., 2020).

In the domain of spinal pathology detection, particularly concerning metastatic lesions, the standard of care relied heavily on manual radiological review. This process is inherently subjective and susceptible to fatigue-related errors, particularly given the high volume of slices in modern high-resolution Computed Tomography scans. Unlike pulmonary nodules, which are contrasted against air, spinal lesions often share similar radiodensity profiles with healthy trabecular bone, making them difficult to isolate using standard density-based thresholding algorithms. While commercial computer-aided detection platforms exist – such as "syngo.via" (Siemens Healthineers) or "Bone VCAR" (GE Healthcare) – these proprietary solutions are often prohibitively expensive and restricted to closed hardware ecosystems (Ha et al., 2017). Furthermore, they typically rely on semi-automated methods that require manual initialisation or seed placement, limiting their utility for fully automated, high-throughput screening compared to end-to-end deep learning approaches (Hammon et al., 2013).

Finally, a distinct technological gap existed in the workflow for 3D anatomical reconstruction. While sophisticated open-source platforms for volumetric segmentation, such as 3D Slicer and ITK-SNAP, were widely accessible, their utility was primarily engineered for diagnostic visualisation rather than manufacturing (Kikinis et al., 2014; Yushkevich et al., 2006). Consequently, the raw surface meshes extracted by these tools frequently exhibited artifacts inherent to slice-based imaging – such as "stair-casing" or terracing effects – along with internal noise and non-manifold geometries (e. g., holes, self-intersections) that render files unprintable. There was a notable absence of validated, unified protocols to bridge this gap using accessible software. Researchers lacked a standardised methodology to systematically convert these raw digital assets into high-fidelity, printable models that balanced the need for

anatomical precision with the topological requirements of additive manufacturing, often forcing reliance on fragmented workflows or expensive industrial computer-aided design solutions.

This Thesis presents practical innovations in artificial intelligence-based medical image analysis and three-dimensional anatomical reconstruction. Together, the open reconstruction protocol, the segmentation and detection networks, and the custom software application form a coherent, freely available framework that spans data acquisition, artificial intelligence analysis, 3D mesh optimisation, physical fabrication, and educational deployment.

The first major advance comprises the development of deep learning tools for detection and segmentation to separate morphological structures across several imaging domains, addressing the "Annotation Bottleneck" described above. In the context of radiological analysis, the Thesis utilises U-Net models to separate individual vertebrae and classify metastatic lesions in full-resolution computed tomography scans. A key novelty is the introduction of a human-in-the-loop methodology, which iteratively combines artificial intelligence predictions with expert refinement. This approach drastically reduces the time-cost of creating "gold standard" datasets compared to manual annotation. Regarding histological analysis, the Thesis introduces an oriented-box adaptation of the YOLOv11 architecture for the quantification of interstitial cells of Cajal. This specific "nano" model (YOLOv11n-obb) is capable of recognising cells on gigapixel histological slides in real time on standard graphics hardware. This pipeline is supplied as "MorpHista", an open-source program developed in this work that performs tissue masking, inference, post-processing, and quantitative reporting.

The second major advance focuses on 3D anatomical reconstruction and educational integration, establishing a fully documented workflow that transforms data from clinical computed tomography, micro-computed tomography, structured-light scanning, and photogrammetry into anatomically verified, print-ready surface meshes using only open-source software. Newly written repair and simplification steps were developed to reduce printing time while maintaining geometric fidelity. All protocols, parameters, and decision criteria have been published, ensuring that both the workflow and its results can be fully reproduced. Following technical validation, this workflow was subjected to educational validation by being integrated into an undergraduate anatomy course. The pedagogical impact was quantitatively verified: students who learned with the specific three-dimensional printed models generated by this pipeline achieved higher practical scores than earlier cohorts who relied on traditional methods.

Ultimately, this research democratises access to advanced medical imaging technologies. By demonstrating that sophisticated analysis and reconstruction techniques can be implemented with modest resources and shared transparently, the work significantly lowers the technical and financial barriers to innovation. The resulting framework offers a robust

solution for the automated detection of spinal pathologies and the streamlined production of patient-specific educational tools, effectively bridging the gap between theoretical deep learning models and practical application in clinical and academic settings.

1 Materials and Methods

1.1 Development and Validation of a 3D Anatomical Model Reconstruction and Printing Protocol

The development and validation of a robust protocol for 3D anatomical model reconstruction and printing formed a cornerstone of this research, aiming to create accurate, accessible, and educationally valuable physical models from diverse imaging sources. This protocol encompassed a multi-stage workflow, from the initial acquisition and preparation of data, to the reconstruction, optimisation, and anatomical validation of a digital model, and finally, physical realisation via 3D printing and subsequent evaluation.

1.1.1 Data Acquisition and Preparation for 3D Reconstruction

The generation of accurate and functionally relevant 3D anatomical models is fundamentally dependent on the quality and characteristics of the acquired initial data and its subsequent preparation. This section delineates the methodologies employed for data acquisition from various sources and the preparatory steps undertaken to render these data suitable for the 3D model reconstruction pipelines.

The data sources integral to this investigation were diverse, reflecting a multimodal approach to capture anatomical information. These sources included digital images obtained through conventional photographic techniques, cross-sectional volumetric data derived from advanced medical imaging modalities such as CT and MRT, and surface geometry data acquired via dedicated 3D scanning technologies.

A significant component of the study, particularly concerning the educational intervention, involved the utilisation of digital images and interactive 3D visualisations facilitated by the “Anatomage” (Kavvadia et al., 2023). This system served as a rich repository, providing access to an extensive case library. The database included over 100 high-resolution cross-sections meticulously derived from four prepared human cadaveric specimens, equally distributed between male and female subjects. Furthermore, it contained data from over 50 diverse clinical cases, presenting a variety of visualisation options such as X-rays, CT, and MRT scans. This digital resource enabled students to engage with complex anatomical structures in a virtual environment, facilitating identification and study.

For the creation of physical, tangible 3D printed anatomical models, data acquisition was pursued through three primary techniques: photogrammetry, µCT, and optical 3D scanning of natural anatomical specimens. The selection of the specific data acquisition modality was a deliberate decision, contingent upon the inherent characteristics of the anatomical structure

targeted for modelling and the requisite level of morphological detail and dimensional accuracy for the intended application.

The initial preparation of the acquired data was a critical phase, with the specific procedures varying based on the data source. Photographic data intended for photogrammetric processing underwent meticulous post-processing to optimise image quality, ensuring clarity and sharpness essential for accurate 3D reconstruction. Medical imaging data, typically formatted according to the Digital Imaging and Communications in Medicine (DICOM) standard (Bidgood et al., 1997), necessitated import into specialised software platforms designed for medical image analysis and manipulation before further processing could commence. Data captured by dedicated 3D scanners also required initial processing, often involving proprietary software bundled with the scanning hardware, to generate preliminary digital representations.

The foundation for the reconstruction of 3D anatomical models was laid by data obtained through distinct acquisition methods: photogrammetry, μCT, and dedicated 3D scanning. Each method yielded data with unique characteristics, necessitating tailored processing pipelines for effective model generation.

Photogrammetry utilised in this research, involved the systematic acquisition of a series of two-dimensional photographic images capturing a natural anatomical specimen from multiple overlapping perspectives. A high-resolution “Sony, ILCE-7RM2” camera coupled with a “Sigma, 70 mm F2.8 DG MACRO Art” lens was the primary equipment for image capture. Specific photographic parameters were meticulously controlled, including an aperture of f/8.0, a shutter speed of 1/640s, and an ISO sensitivity of 100. The camera’s sensor, boasting a resolution of 42.3 megapixels, was instrumental in obtaining images with sufficient detail to support high-quality texture mapping on the resulting 3D models. The pursuit of optimal sharpness and clarity in the images was paramount, frequently requiring the use of a stable tripod and supplementary artificial light sources to minimise motion blur and ensure consistent illumination. Subsequent to image acquisition, raw photographic data underwent a rigorous post-processing workflow utilising “Adobe Photoshop” (version 23.1.1) and “Capture One 22 Pro” (version 15.0.1.4) software. This process involved adjustments to parameters such as saturation, contrast, and overall colour balance to enhance image quality and prepare the data for photogrammetric software.

μCT provided detailed cross-sectional volumetric data, offering insights into both the external morphology and internal structure of specimens. A “Scanco Medica, μCT50” machine was utilised for this purpose, operating under precisely defined scanning parameters. The scanned area was configured as a cylinder with a diameter of 48 millimetres and a height

of 110 millimetres. The X-ray energy was set at 90 peak kilovoltage, with an intensity of 88 microampere, and filtration was achieved using a 0.5 millimetres aluminium filter. High-resolution presets were consistently applied, resulting in a field of view (FOV) of 49.6 millimetres, a voxel size of 24.2 micrometres, and an integration time of 1500 milliseconds. Initial processing of the raw μCT data was performed using the proprietary software supplied with the μCT machine. The processed data was subsequently exported in the standardised DICOM file format, which is widely compatible with medical imaging software and necessary for the subsequent 3D model creation workflow. An additional source of CT data was utilised from the "New Mexico Decedent Image Database" project (Edgar et al., n.d.). This database provided CT scans acquired using a specific protocol characterised by a peak kilovoltage of 120, milliampere-seconds of 200, a scan length ranging from 800 to 1000 millimetres, a scan FOV of 500 millimetres, a pitch of 0.942, collimation of 16 × 0.75, a rotation time of 1.0 s, and a matrix size of 512 × 512. These scans were reconstructed with varying slice thicknesses and image counts optimised for visualising either soft tissue or bone (3 millimetres × 3 millimetres, 320 images, 1 millimetres × 0.5 millimetres, 1900 images).

3D scanning was performed using a "Shining3D, EinScan-S". This method captured the external surface geometry of physical objects without providing internal structural information. The scanning procedure involved capturing 36 individual pictures while the specimen was rotated on a turntable. The turntable speed was set to 1, and a half turn was performed to capture sufficient data for reconstruction. This technique is particularly well-suited for obtaining detailed surface models of objects with accessible external features.

1.1.2 3D Reconstruction Pipelines

The transformation of raw data acquired from diverse sources, including photogrammetry, μCT, and 3D scanning, into usable 3D anatomical models necessitated the implementation of distinct computational pipelines. Each pipeline was specifically designed to process the unique characteristics of the input data, ultimately yielding digital 3D mesh models suitable for further manipulation and application, such as physical fabrication through additive manufacturing.

For data obtained via photogrammetry, the reconstruction workflow was centred around specialised software capable of processing multiple overlapping two-dimensional images to generate a dense point cloud and subsequently a mesh. This pipeline involved importing the photographic images, aligning them based on common features, defining the region of interest for reconstruction, and generating a high-detail mesh. A critical subsequent step was the application of texture derived from the original photographs onto the generated mesh,

creating a visually realistic 3D model. Topological defects inherent in the initial mesh generation, such as non-manifold geometry or holes, were identified and addressed within this pipeline to ensure model integrity.

Each protocol parameter was first set to its default value, then systematically varied by ± 50 % of that baseline, and the resulting outputs were benchmarked against the default case (Edelmers et al., 2021). The entire protocol was validated using 3D models of the foot bones.

Photogrammetry Protocol

1 Launch the "RealityCapture" program
2 Import images into the program
3 Adjust alignment settings:
  3.1 Max feature per mpx.: 20000
  3.2 Max features per image: 80000
  3.3 Preselector features: 20000
  3.4 Image overlap: low
  3.5 Force component rematch: yes
  3.6 Detector sensitivity: high
4 Launch the alignment process
5 Define the reconstruction region
6 Use reconstruction with "High detail" option to initialise the meshing process
7 Use "Clean Model" tool to remove topology defects (non-manifold vertices, non-manifold edges, holes, isolated vertices)
8 Use the "Texture" instrument with the following setting to create a texture for the model:
  8.1 Imported-model default texture resolution: 16384 × 16384
  8.2 Correct colours: Yes
9 Export the 3D model along with the texture as an .obj object.

The pipeline for processing medical imaging data, particularly from CT scans, involved a different approach. Following the initial acquisition and export of data in DICOM format, the primary step was segmentation, that is the process of isolating specific anatomical structures (for example, bones, organs) from the surrounding tissues within the volumetric data. This was achieved through various techniques, including thresholding based on voxel intensity values, manual drawing, and automated or semi-automated methods. In instances where a single anatomical structure spanned across multiple image series, an initial step of merging these series was required to create a continuous volume before segmentation could be performed.

The segmented data was then used to generate a surface mesh representing the boundaries of the isolated anatomical structure.

Series Merging Protocol

Data import

1 Start the “3D Slicer” software;
2 Access the “DICOM” database;
3 Choose the appropriate patient;
4 Identify two series intended for later merging;
5 Import the identified series.

Creation of region of interest (ROI)

1 Activate the “Crop Volume” module;
2 Under “Input Volume”, choose a series;
3 Under “Input ROI”, opt for “Create ROI”. The resulting volume will be named “Crop Volume” ROI;
4 Click the “Center View” button in the 3D visualisation window;
5 Select the “Fit to Volume” option;
6 Resize the ROI to ensure both loaded volumes, presented as two individual entities, fit within this new ROI.

The process of stitching two volumes

1 Access the “Stitch Volume” module;
2 Under Stitched “Volume ROI”, select the “Crop Volume” ROI you previously created;
3 For “Original Volume 1”, choose the primary volume to which the secondary volume will be appended;
4 For “Original Volume 2”, select the other loaded volume;
5 Click the “Create Stitched Volume” button.

Manual Segmentation Protocol

1 Launch the “3D Slicer” program
2 Import CT data into the program:
  2.1 Set the image contrast to ensure better visibility.
3 Add a new segment using the tool:
  3.1 Segment Editor:
    3.1.1 Set up the “Threshold” tool
    3.1.2 Using “Scissors”, “Draw”, “Islands”, manually segment the required structure

4 When segmenting one structure is complete, proceed to the second one by adding a new segment and repeat the segmentation procedure if needed

5 Export the completed segment or segments as a 3D model in the .obj file format.

Segmentation Protocol with Total Segmentation module

1 For “Input Volume”, choose the volume you have loaded

2 In “Segmentation Tasks”, opt for “Total”

3 Click the “Apply” button. Deletion of unnecessary data

4 Remove all items, retaining only the volume used in the prior step and the desired semantic segmentations of anatomical structures:

4.1 Masks validation and correction

5 When smoothing is necessary:

5.1 For the “Smoothing Method”, select “Median”

5.2 Set the “Kernel Size” to 3.00 millimetres

5.3 Toggle the “Apply to Visible Segments” option to “Enable”

6 Verify the morphological accuracy of segmented structures using references from literature or digital platforms. If required, adjust utilising the “Draw”, “Paint” (with the “Sphere Brush” feature activated), “Erase”, and “Scissors” tools

7 If there is a segmentation error where a part of one structure is identified as a segment of another bone, follow these steps to merge and rectify:

7.1 In the “Data” module, duplicate the segment that contains a section of the incorrect bone

7.2 Utilise the “Scissors” tool from the “Segment Editor” module to remove everything except the mislabelled structure

7.3 Using the “Logical Operators” tool, integrate the two segments of a single structure using the “Add” operation

7.4 Data export

8 Save the volume in .nrrd file format

9 Save segmentation for the volume in .seg.nrrd file format.

For data acquired directly from a 3D scanner, the initial output was typically a point cloud or a preliminary mesh representing the surface geometry of the scanned object. This data then entered a processing pipeline focused on refining the mesh, aligning multiple scans if necessary, and preparing the model for subsequent stages such as optimisation and printing.

Each of these pipelines culminated in the creation of a digital 3D model, typically represented as a mesh (a collection of vertices, edges, and faces defining the shape of

the object). These models then served as the basis for further processing steps aimed at optimising their geometry and preparing them for specific applications, most notably 3D printing.

1.1.3 Tools and Software for 3D Reconstruction

The execution of the 3D reconstruction pipelines, and the subsequent processing of the resulting models relied on a comprehensive suite of software tools and specialised hardware (Table 1.1 and 1.2). The selection of these tools was driven by the specific requirements of each stage of the workflow, from data acquisition to the preparation for physical output. A notable aspect of the software utilised is the availability of several powerful programs at no cost for scientific and research purposes, enhancing the accessibility of these advanced methodologies.

Table 1.1

List of used hardware

Equipment	Manufacturer	Model	Specification / URL (access date)
Camera	Sony	ILCE-7RM2	electronics.sony.com/imaging/interchangeable-lens-cameras/full-frame/p/ilce7rm2-b (accessed 17 Aug 2022)
Lens	Sigma	70 mm F2.8 DG MACRO Art	sigma-global.com/en/lenses/a018_70_28 (accessed 17 Aug 2022)
µCT	SCANCO Medical	µCT 50	scanco.ch/microct50.html (accessed 17 Aug 2022)
Computer	Lenovo	Legion 7	windows 11 Pro; AMD Ryzen 7 5800H; NVIDIA GeForce RTX 3080 16 gigabyte; 64 gigabyte DDR4 3200 megahertz; 1 terabyte solid-state drive.
3D Scanner	Shining 3D	EinScan-S	einscan.com/desktop-3d-scanners/EinScan-Se/EinScan-Se-specs (accessed 17 Aug 2022)

Table 1.2

List of used software

Software / Platform	Version	Information / URL (access date)
EinScan-S	2.5.0.7	einscan.com/support/download/software/?scan_model=EinScan-S (accessed 17 Aug 2022)
µCT	– / –	shipped along with the µCT 50 machine
3D Slicer	5.02	slicer.org (accessed 17 Aug 2022)
MeshLab	2022.02	meshlab.net (accessed 17 Aug 2022)
Meshmixer	3.5.474	meshmixer.org (accessed 17 Aug 2022)
Ultimaker Cura	4.8	ultimaker.com/software/ultimaker-cura meshmixer.org (accessed 17 Aug 2022)
RealityCapture	1.2.0.17385	capturingreality.com/RealityCapture (accessed 17 Aug 2022)
Adobe Photoshop	23.1.1	for textures colour correction
Capture One 22 Pro	15.0.1.4	for cameras RAW-image processing
Sketchfab	– / –	sketchfab.com (accessed 17 Aug 2022)

For the reconstruction of 3D models from photographic data using photogrammetry, “RealityCapture” served as the primary software platform, which is specifically designed for creating 3D models from images and/or laser scans, offering functionalities for camera alignment, dense point cloud generation, mesh creation, and texturing. Its graphical user interface and integrated tools facilitated the implementation of the photogrammetry protocol.

The processing and segmentation of medical imaging data, particularly CT scans, were performed using “3D Slicer” (Kikinis et al., 2014). This open-source software platform is widely recognised in the field of medical image analysis and visualisation. It provided the necessary tools for importing datasets in DICOM format, adjusting visualisation parameters such as image contrast, and performing both manual and automated segmentation of anatomical structures. The “Segment Editor” module within “3D Slicer” offered a range of tools, including “Threshold”, “Scissors”, “Draw”, “Smooth”, and “Islands”, for precise segmentation. For tasks involving the merging of multiple image series, the Crop Volume and Stitch Volume modules within “3D Slicer” were employed. Additionally, the “TotalSegmentator” module (Wasserthal et al., 2023) facilitated automated semantic segmentation of numerous anatomical structures.

For the crucial processes of mesh simplification and optimisation, “MeshLab” (versions 2022.02 and 2020.12) was a key tool (Cignoni et al., 2008). This open-source software is specifically designed for processing and editing unstructured 3D meshes. It provided a comprehensive set of filters and tools for cleaning up mesh artifacts, such as duplicate faces or vertices, repairing non-manifold geometry, and simplifying the mesh (reducing the number of polygons) while striving to maintain the original shape and topological integrity.

Further model editing and optimisation capabilities were provided by “Meshmixer”. This software offered intuitive tools for selecting and manipulating specific areas of the mesh, including functions for erasing, filling holes, sculpting, making solid objects, and combining multiple meshes. It was particularly useful for addressing small defects like micro-holes and for performing mesh remeshing and smoothing operations to refine the model’s surface.

The final stage of preparing digital models for physical fabrication involved “Ultimaker Cura” to prepare the 3D models for printing on FDM machines. This software allowed for the configuration of numerous printing parameters, including layer height, infill density and pattern, shell thickness, support structures, and build plate adhesion. The “Auto-Orientation” extension within Cura assisted in optimally positioning the model on the build platform.

Additional software used in the data acquisition and preparation phases included “Adobe Photoshop” for texture colour correction and “Capture One 22 Pro” for processing

RAW images from the camera. The “Sketchfab” platform served as a means for publishing and presenting the completed digital 3D models.

The hardware employed for data acquisition included a “Sony, ILCE-7RM2” camera with a “Sigma, 70 millimetres F2.8 DG MACRO Art” lens for photogrammetry, a “SCANCO Medical, µCT50” machine for µCT, and a “Shining3D, EinScan-S” 3D scanner for optical scanning. The computational tasks were performed on a “Lenovo Legion 7” computer system, equipped with a “Windows 11 Pro” operating system, an “AMD, Ryzen 7 5800H” processor, an “NVIDIA, GeForce RTX3080” graphics card, 64 gigabyte of double data rate 4 small-outline dual-inline memory module 3200 megahertz random access memory, and a 1000 gigabyte solid-state drive, providing ample processing power and memory for handling large 3D datasets.

1.1.4 3D Model Optimisation, Anatomical Validation, and 3D Printing Preparation

Subsequent to the successful reconstruction of 3D anatomical models, a critical phase of optimisation and preparation was undertaken to ensure the models were suitable for their intended applications, particularly physical realisation through 3D printing. This involved refining the mesh geometry, ensuring structural integrity, and configuring parameters specific to the additive manufacturing process.

Model optimisation primarily focused on improving the mesh quality and reducing file size without compromising anatomical accuracy or essential detail. This was achieved through a series of steps utilising “MeshLab” and “Meshmixer” software. Initial optimisation in “MeshLab” involved the systematic removal of topological errors and artifacts that may arise during the reconstruction process. This included identifying and eliminating isolated mesh components, duplicate faces and vertices, zero-area faces, and repairing non-manifold edges and vertices. These cleaning operations were essential for creating a watertight and structurally sound mesh, which is a prerequisite for successful 3D printing. Mesh simplification was also performed, particularly for models intended for online platforms with file size limitations. The quadric edge collapse decimation technique in “MeshLab” was applied to reduce the polygon count while preserving the model’s boundary, normals, topology, and planar features.

Each protocol parameter was first set to its default value, then systematically varied by ± 50 % of that baseline, and the resulting outputs were benchmarked against the default case (Edelmers et al., 2021). The entire protocol was validated using 3D models of the foot bones.

Simplification and Optimisation Protocol

1 Launch the “MeshLab” program

2 Import a 3D model into the program

3 Remove artifacts, simplify, and optimise the model using tools (all the default values with modifications indicated below)
    3.1 Remove isolated pieces (wrt diameter)
    3.2 Remove duplicated faces
    3.3 Remove duplicated vertex
    3.4 Remove zero area faces
    3.5 Repair non-manifold edges by removing faces
    3.6 Repair non-manifold vertices by splitting
    3.7 Remove unreferenced vertices
    3.8 Simplification: quadric edge collapse decimation:
        3.8.1 Preserve boundary of the mesh: on
        3.8.2 Preserve normal: on
        3.8.3 Preserve topology: on
        3.8.4 Planar simplification: on
        3.8.5 Remeshing: isotropic explicit remeshing
4 Adaptive remeshing: on
5 Collapse step: off
6 Export the completed segment or segments as a 3D model in the binary .ply file format.

Further refinement and optimisation were conducted in “Meshmixer”. This included addressing smaller geometric imperfections, such as micro-holes, by reconstructing the mesh surface in the affected areas. The “Inspector tool” with a “Smooth Fill” mode was employed for this purpose, with a small threshold value to target only minor gaps. The “Remesh tool” in “Meshmixer” was utilised to optimise the polygon distribution and density, often aiming for a more uniform mesh structure which can be beneficial for printing quality and file size management. Smoothing operations were also applied to the model surface as needed to reduce jaggedness and improve the visual appearance, using a shape-preserving smoothing type to avoid distorting the underlying anatomy.

Optimisation Protocol

1 Launch the “MeshLab” program
2 Import the 3D model into the program
3 Remove artifacts using tools:
    3.1 Remove Duplicated Faces
    3.2 Remove Duplicated Vertex
    3.3 Remove Zero Area faces

3.4 Repair Non-Manifold Edges by removing faces

3.5 Repair Non-Manifold Vertices by Splitting

3.5.1 Vertex Displacement Ratio = 0

3.6 Remove Unreferenced Vertices

3.7 Remove Isolated Pieces (wrt Diameter)

3.7.1 Max diameter of isolated attachments (%) = 10

3.7.2 Remove Unreferenced Vertices = ON

4 Export 3D model as an OBJ file

5 Launch the “Meshmixer” program

6 Import the 3D model into the application

7 Close micro-holes (boundary edge type error) by reconstructing the mesh surface using the instrument:

7.1 Inspector

8 Hole Fill Mode = Smooth Fill

9 Small Thresh = 0.01 millimetres

10 Optimise the model polygon mesh to minimise the size of the file (3D model) using tools

11 Remesh:

11.1 Remesh Mode = Relative Density

11.2 Density (%) = 0

11.3 Regularity = 100

11.4 Iterations = 10

11.5 Transition (millimetres) = 0

11.6 Smooth Group Boundaries = ON

11.7 Boundary Mode = Refined Boundary

12 Smooth the 3D models surface if needed

13 Select

14 Deform

15 Smooth:

15.1 Smoothing Type = Shape Preserving

15.2 Smoothing = 1

15.3 Smoothing Scale = 4 (decrease or increase as needed)

15.4 Constraint Rings = 3

16 Export the 3D model as an .obj file.

A crucial aspect of the workflow was the manual validation of the digital models against anatomical literature (Motsinger, 2020). If discrepancies were identified, an editing methodology utilising "Meshmixer" was employed to make necessary adjustments to the digital model to ensure anatomical correctness. This involved using tools like "Select", "Edit" ("Erase & Fill", "Discard"), "Brushes", "Make Solid", and "Add Tube" to modify the mesh geometry. The ability to combine multiple models within "Meshmixer" was also valuable for reconstructing complex anatomical regions from individual components.

Validation Protocol

1. Check the correctness of anatomical structures using the literature (Motsinger, 2020)
2. For 3D models whose structures do not correspond to normal human anatomy, make the necessary adjustments using the "Editing Methodology"
3. Launch the "Meshmixer" program
4. Import the 3D model (or models if there is a need to combine multiple models into a single model, such as putting a foot from individual bones) into the program
5. Use instruments to make necessary adjustments:
    - 5.1 Select
    - 5.2 Edit
    - 5.3 Erase & Fill
    - 5.4 Discard
    - 5.5 Brushes
    - 5.6 Make Solid
    - 5.7 Add Tube
6. To combine multiple models into one, select all models in the "Object Browser" section by holding the "Shift" button on the keyboard and select all the models from the list by clicking on them with a cursor; then, apply the "Combine" tool
7. Export the 3D model as an .obj file.

The final stage involved preparing the optimised digital models for physical fabrication using FDM 3D printers. This was managed through "Ultimaker Cura" slicing software. Importing the 3D model into "Ultimaker Cura" allowed for the configuration of numerous print settings that directly influence the physical properties and appearance of the printed object. A custom print profile was developed, based on a high-quality "Visual" profile with a 0.1 millimetres slice thickness, and further tailored to optimise print quality, structural durability, and dimensional precision. Key parameters included setting a wall line count of 10 for the outer shell, selecting a concentric pattern for the top and bottom layers, and randomising the Z seam

alignment to minimise its visibility. The internal structure was defined by an infill density of 30 % and a gyroid infill pattern, providing a balance between material usage and structural support. Build plate adhesion was enhanced using a brim, printed with PVA material from the second extruder, to ensure the model adhered securely to the build platform during printing. The "Auto-Orientation" extension was used to automatically position the model on the build plate in an orientation that minimised the need for support structures and optimised print quality.

3D Printing Protocol | Cura Ultimaker

1 Launch the "Ultimaker Cura" program
2 Import the 3D model into the program
3 Create a profile (based on the built-in profile "Visual" with a slice thickness of 0.1 millimetres with further modification and optimisation to maximise quality, durability, and precision); the main material for the model is PLA, in its turn for the support structures the PVA is being used
4 Shell:
  4.1 Wall Line Count = 10
  4.2 Top/Bottom Pattern = Concentric
  4.3 Z Seam Alignment = Random
5 Infill:
  5.1 Density (%) = 30
  5.2 Infill Pattern = Gyroid
6 Build Plate Adhesion:
  6.1 Build Plate Adhesion Type = Brim
  6.2 Build Plate Adhesion Extruder = Extruder 2 (PVA)
7 Optimise models' position using the "Auto-Orientation" extension from the "Ultimaker Cura" library (Marketplace)
8 Start the printing process
9 Remove support structures from the model by immersing it into the water (25°C) for 24 h
10 Remove the 3D model from the container with water and allow it to dry
11 Check the correctness of the 3D printed model by comparing it to the virtual original.

The physical printing was performed on two models of FDM printers: "Prusa i3 MK2" and "Ultimaker S5". The primary material for the anatomical models was PLA, a widely used biodegradable thermoplastic. For support structures, polyvinyl alcohol (PVA) was utilised due to its water-soluble properties, allowing for easy removal after printing. Post-processing of

the printed models involved immersing them in water at 25℃ for 24 hours to dissolve the PVA support material, followed by drying. The final step was a visual and tactile inspection of the 3D printed model, comparing it against the virtual original to verify its correctness and quality.

Figure 1.1 illustrates the complete process of 3D reconstruction through to the printed model.

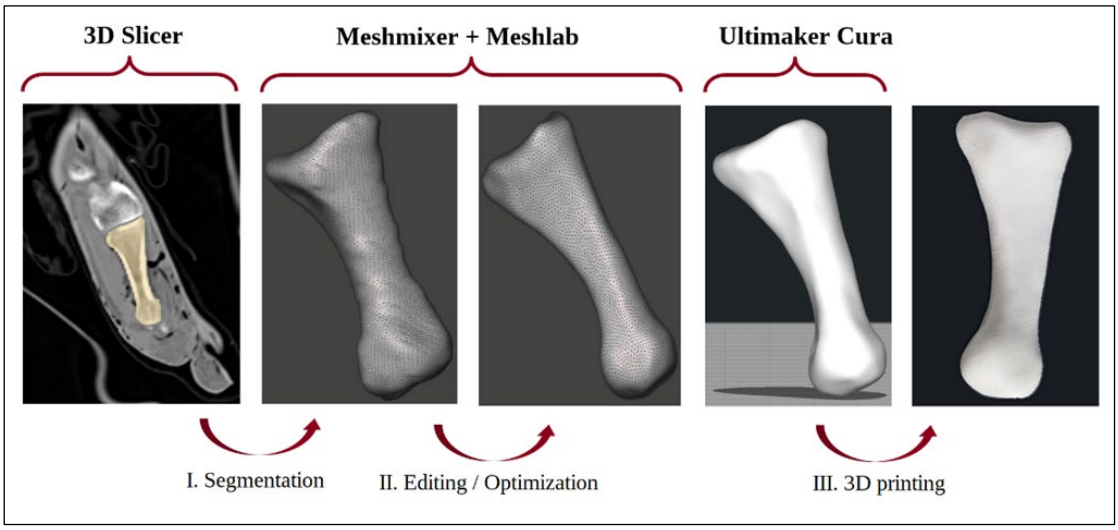

Figure 1.1. **Graphical representation of 3D reconstruction protocol**

1.2 Methodologies for AI-Driven Morphological Analysis

The methodologies for AI-driven morphological analysis were developed to automate and enhance the detection, segmentation, and quantification of anatomical and cellular structures within medical images. This involved curating specific datasets, selecting and adapting suitable deep neural network architectures, and implementing rigorous training and evaluation procedures.

1.2.1 Datasets for Development and Evaluation of AI Models

The foundation of this research relies upon comprehensive datasets appropriate for the training and evaluation of AI models in medical image analysis. Two distinct datasets were employed to address the specific objectives of adapting classification networks for segmentation and detecting spinal metastatic lesions.

The research on AI-assisted detection and localisation of spinal metastatic lesions utilised two separate datasets. The first dataset, designated for vertebra segmentation, consisted of CT scans from 115 patients presenting with polytrauma but relatively undamaged spines. These full-body CT scans were acquired at the “Riga East University Hospital” (RAKUS) hospital (2-PĒK-4/97/2022, 21 February 2022). The second dataset, focused on metastasis

detection, contained CT scans from 38 patients diagnosed with spinal metastases (Edelmers, 2024). Following manual segmentation by medical professionals using “3D Slicer” software (Kikinis et al., 2014), the data were converted from DICOM format to a NRRD format to enhance input/output efficiency during model training.

For the estimation of Cajal cells in the anal canal wall, a retrospective cohort study was conducted involving forty-two patients. Forty-two formalin-fixed and paraffin-embedded (FFPE) anorectal tissue samples were collected. From whole slide images (WSIs) depicting immunohistochemically detected ICCs, 40 patches with a resolution of 2048×2048 pixels were extracted. These images were initially obtained at maximum magnification. To align with the input requirements of the YOLOv11n-obb architecture (Khanam & Hussain, 2024), each 2048×2048 patch was divided into four smaller 1024×1024 sections, resulting in a total of 160 images. All these images were annotated, yielding 1871 labelled masks for training purposes.

The datasets were specifically prepared to serve as input for the training of the AI models developed in this research. The preparation involved several crucial steps to ensure data quality, consistency, and suitability for the chosen deep neural network architectures.

In the context of spinal metastasis detection, two U-Net-based networks were trained. The first network was trained using the CT scans from 115 polytrauma patients with relatively undamaged spines for the task of spine localisation and vertebra segmentation. The second network, dedicated to the instance segmentation and classification of metastatic lesions (lytic and sclerotic), was trained on the CT scans from the 38 patients diagnosed with spinal metastases. The dataset consists of 19456 images, each with a resolution of 512×512 pixels. The nnU-Net library’s built-in augmentation capabilities were utilised, which include a wide array of transformations such as rotations, scaling, Gaussian noise, Gaussian blur, adjustments in brightness and contrast, low-resolution simulation, gamma correction, and mirroring (Isensee et al., 2021). These augmentations were applied adaptively based on dataset characteristics, enhancing the model’s robustness and generalizability. The dataset for metastasis detection was meticulously curated with manually created segmentation masks.

For the Cajal cell estimation using the YOLOv11n-obb architecture, a dataset comprising 160 images (derived from 40 WSIs) with 1871 labelled masks was used for training (Edelmers, 2025). The training dataset was further enhanced through rotation and flipping augmentation techniques to improve the model’s robustness against variations in immunostaining intensities. The final dataset split for this task included 376 augmented images for training and 32 non-augmented images for validation.

1.2.2 Deep Neural Network Architectures

Deep neural networks constitute the core methodological framework employed in this research for medical image analysis tasks, specifically focusing on segmentation simulation, spinal lesion detection, and cell estimation. The selection and adaptation of these networks were guided by the specific requirements of each task, balancing performance, computational efficiency, and interpretability.

For the AI-assisted detection and localisation of spinal metastatic lesions, a multi-network approach based on the U-Net architecture was adopted. U-Net is a convolutional network architecture specifically designed for biomedical image segmentation, characterised by its symmetric encoder-decoder structure and skip connections that facilitate the transfer of spatial information from the encoder to the decoder. Two U-Net-based networks were employed: one for spine localisation and vertebra segmentation, and another for the instance segmentation and classification of metastatic lesions. This dual-stage approach allows for hierarchical processing, first localising the region of interest (the spine) and then focusing on the detailed segmentation and classification of lesions within that region. The implementation utilised the nnU-Net framework, which provides a self-configuring method for biomedical image segmentation, automating many aspects of the pipeline.

The selection of the YOLOv11n-obb architecture for the estimation of ICC was driven by the specific morphological characteristics of these cells and the computational exigencies of high-throughput digital pathology. Unlike generic object detection tasks where subjects are typically upright and compact, ICCs present as spindle-shaped or stellate structures with high aspect ratios and arbitrary orientations within the tissue matrix. Standard object detection models, such as the traditional YOLO series or Faster R-CNN, utilise horizontal bounding boxes which are axis-aligned. When applied to diagonally oriented, elongated cells, horizontal bounding boxes inevitably encompass significant background noise (non-cellular stroma) to capture the full extent of the cell, leading to a low signal-to-noise ratio that degrades classification accuracy (Ma et al., 2018).

Furthermore, the density of cellular clusters in histological samples presents a critical failure mode for HBB-based detectors. When two elongated cells lie in close proximity but at different angles, their respective horizontal bounding boxes frequently exhibit high IoU overlap. This overlap inadvertently triggers non-maximum suppression algorithms – designed to eliminate duplicate detections – to suppress valid cell instances, resulting in systematic undercounting (Neubeck & Van Gool, 2006). The YOLOv11n-obb architecture addresses this by introducing an angular parameter to the regression head, allowing the bounding box to rotate and align tightly with the cell's principal axis. This oriented approach drastically minimises

background inclusion and effectively resolves the “overlapping instance” problem, ensuring that closely packed cells are distinctively recognised.

In terms of computational scale, the analysis of WSI imposes severe constraints on model complexity. A standard histological slide digitised at 40x magnification yields gigapixel-scale data that must be tiled into thousands of patches for inference. Utilising heavy architectures with massive parameter counts, such as those based on ResNet-101 or DenseNet backbones, would introduce prohibitive latency, rendering the system impractical for clinical or large-scale research workflows (Litjens et al., 2017). The “Nano” variant of YOLOv11 was selected specifically to mitigate this bottleneck. With a highly optimised backbone containing approximately 2.6 million parameters, it enables rapid inference speeds suitable for real-time screening of massive histological datasets without necessitating specialised high-performance computing clusters (Khanam & Hussain, 2024).

Despite its compact size, the YOLOv11 architecture integrates advanced feature aggregation mechanisms that are superior to previous lightweight iterations. It employs improved Cross-Stage Partial networks and Spatial Pyramid Pooling – fast modules to enhance multi-scale feature fusion (Khanam & Hussain, 2024). This is particularly relevant for ICC detection, as the apparent size of the cells can vary depending on the sectioning plane of the tissue. By preserving high-resolution features through the network layers, the YOLOv11n-obb model maintains high sensitivity for small, thin cellular processes that are often lost in the down-sampling layers of older architectures, thus achieving a state-of-the-art balance between geometric precision and computational efficiency.

The spinal metastasis detection research employed U-Net-based architectures, implemented within the nnU-Net framework. The U-Net architecture features a contracting path (encoder) that captures context and an expansive path (decoder) that enables precise localisation. Skip connections between corresponding levels of the encoder and decoder paths are fundamental to U-Net, allowing the decoder to utilise high-resolution features from the encoder, which is vital for accurate segmentation in medical images. The specific U-Net implementation within nnU-Net included several key design choices: instance normalisation instead of batch normalisation to handle smaller batch sizes common in 3D medical imaging, leaky ReLU activation functions to introduce non-linearity and prevent dying neurons, and deep supervision with topology-adapted parameters. These choices were made to optimise the architecture for the complex and heterogeneous nature of spinal metastases and to maintain spatial precision.

1.2.3 Training Procedures, Hyperparameter Tuning, and Evaluation Metrics

The training of the deep neural networks involved carefully defined procedures and systematic hyperparameter tuning to achieve optimal performance for each specific task.

The training of the U-Net-based networks for spinal metastasis detection was managed by the nnU-Net framework, which employs an automated parameterisation approach combining fixed, rule-based, and empirical parameters to adapt to diverse datasets.

Fixed parameters included the architecture template, based on a U-Net-like structure with two convolutional blocks per resolution level and instance normalisation. Training typically ran for 1000 epochs, with 250 minibatches per epoch. The learning rate followed a polynomial decay from an initial value of 0.01 and was reduced throughout training. Optimisation was performed using stochastic gradient descent with Nesterov momentum ($\mu = 0.99$). The loss function utilised was a combined Dice and cross-entropy loss, balancing accuracy for foreground-background segmentation and boundary precision.

Rule-based parameters were determined by nnU-Net's dataset fingerprinting, which analyses characteristics such as voxel spacing and median image shape. For anisotropic datasets, anisotropic resampling was employed using the tenth percentile of the lowest resolution axis. Patch size was initially based on the median image shape and adjusted iteratively to fit within graphical processing unit memory constraints. Network topology, including the number of downsampling layers, was adapted based on target spacing and voxel size to ensure an effective receptive field size. Normalisation techniques varied by modality, with z-score normalisation for most cases and specific percentile clipping and z-scoring for CT images.

Empirical parameterisation involved testing post-processing configurations, such as largest-component suppression, to assess their impact on cross-validation performance and remove false positives. Ensemble selection evaluated the performance of different configurations (2D, full-resolution 3D, cascaded 3D U-Net) across cross-validation folds to select the best model or ensemble for predictive robustness.

Four U-Net architecture subtypes were trained: a 2D model using single slices, a 3D low-resolution model with downsampled input, a 3D full-resolution model using original resolution, and a 3D cascade full-resolution model that processed downsampled images for overall structure before refining details with full-resolution data.

For the Cajal cell estimation using YOLOv11n-obb, training was performed on the augmented dataset. Model validation was conducted at the end of each training epoch on a prepared set. During this process, the model's predictions were compared to ground truth

annotations, and non-maximum suppression was applied to eliminate redundant bounding boxes. Key metrics calculated during this phase included precision, recall, and mean average precision (mAP), specifically mAP_{50} (using an intersection over union threshold of 0.5) and mAP averaged over a range of thresholds ($mAP_{50\text{-}95}$). These metrics provided a comprehensive assessment of the model's performance on unseen data, guiding hyperparameter adjustments and serving as checkpoints for selecting the best-performing model.

Results

This section reports the study's findings, emphasising the workflows and outcomes for 3D reconstruction and fabrication of anatomical structures. It also details the educational deployment of these methods and the technical procedures used for model generation and validation.

Results of 3D Anatomical Model Reconstruction and Printing

The work involved the creation of 3D digital models from various sources and their subsequent physical realisation through 3D printing. Different techniques were employed for the initial digital model creation, and a systematic approach was followed for printing and post-processing. The physical realisation of the digital anatomical models was achieved through 3D printing. Specifically, fused deposition modelling (FDM) technology was utilised for the printing process. The printing was conducted using an "Ultimaker 5S" 3D extrusion-type printer. Key parameters were meticulously controlled to ensure print quality and fidelity. These parameters included a nozzle diameter of 0.4 millimetres, a layer height of 0.1 millimetres, a print speed of 70 millimetres per second, a printing temperature of 200℃, a build plate temperature of 60℃, and a fan speed of 100 %. The printing materials comprised a polylactic acid–polyhydroxyalkanoate blend ("Semi-Matte White") for the primary model structures and "Ultimaker PVA" for the soluble support structures. Fabrication of the complete foot-bone set required 44 hours 15 minutes of print time and used 122 grams of a polylactic acid–polyhydroxyalkanoate blend for the models and 45 grams of PVA for the support structures.

Following the printing phase, a crucial post-processing methodology was implemented to prepare the physical models for use. This involved the removal of the soluble support structures. The printed models were immersed in water at 24℃ for 24 hours to dissolve the PVA support material. After the dissolution process, the models were removed from the water and allowed to air dry at room temperature (24℃) for another 24 hours. The final step in the post-processing was a direct comparison between the physically printed model and its corresponding virtual 3D model to assess the outcome of the printing and post-processing steps.

3D printing methodology protocol details the steps taken from preparing the digital model for printing to the completion of the printing process, including the specific printer settings used. The outcome, depicted as a 3D printed model, is illustrated in Figure 1.

Figure 1. **Final physical output after printing and post-processing**

Assessment of Anatomical Accuracy, Print Fidelity, and Model Validation

The creation of anatomically correct and print-optimised 3D models involved a multi-step process beginning with the segmentation of relevant anatomical structures from medical imaging data. For the human foot bones, a total of 28 individual bones were segmented from 763 CT images using the "3D Slicer" application. This segmentation followed a developed methodology to isolate each bone as a separate digital model.

The initial digital models underwent a validation process to ensure anatomical correctness by comparing them against established anatomical literature. Based on this process, adjustments were made to the models using the "Meshmixer" program according to a defined editing methodology. A total of 19 models required modification to align with normal human anatomy.

Following anatomical correction, the models were optimised with the identification and correction of errors as well as artifacts that may have arisen during the segmentation phase. The "MeshLab" program was used for this purpose, addressing issues such as duplicating

points, duplicating faces, faces with zero areas, non-manifold edges and points, vertices not referenced by a face, and microparticles not forming a surface. Subsequently, the on mesh of the models was simplified to improve the visual appearance for virtual library demonstrations, make the mesh suitable for further manipulations (e. g. deformation, cutting), reduce the file size, and ensure the model's printability on an FDM-type printer. All 28 models were optimised to correct segmentation-related errors and artifacts.

Different techniques were explored for creating bone digital 3D models from natural specimens, including 3D scanning, photogrammetry, and μCT which resulted in models with varying characteristics in terms of polygon mesh complexity and texture data (Figure 2).

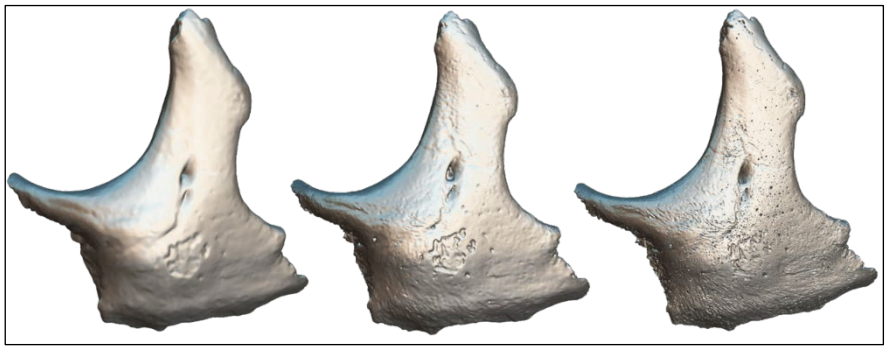

Figure 2. **3D model's simplified and optimized polygon meshes created by using different techniques**

From left to right: 3D scanning, photogrammetry, μCT

The original number of faces and vertices before and after the application of a Simplification and Optimisation Protocol varied significantly depending on the initial reconstruction technique (Table 1).

Table 1

Number of faces and vertices of 3D models before and after application of Simplification and Optimisation Protocol

	Before Simplification		After Simplification	
Techniques	**Faces**	**Vertices**	**Faces**	**Vertices**
3D scanning	700002	350003	no simplification done	
Micro Computed Tomography	70195566	35073613	7019556	3485608
Photogrammetry	13716318	6882203	700842	350423

Similarly, the size of the obtained texture maps differed (Table 2).

Table 2

Size of obtained texture map of 3D models

Techniques	Size of Texture Map in Pixels (Width × Height)
3D scanning	766 × 998
Micro Computed Tomography	No visual data captured
Photogrammetry	16384 × 16384

Visualisation techniques, such as applying an X-ray shader, were used to reveal the internal structures of the digital models (Figure 3).

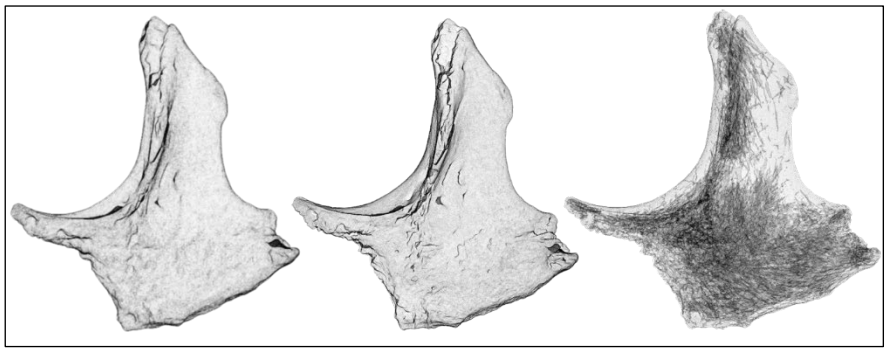

Figure 3. **3D models created by using different techniques with an X-ray shader applied**

From left to righ t: 3D scanning, photogrammetry, μCT

Further rendering and presentation on platforms like "Sketchfab" involved applying shaders, light sources, global illumination, ambient occlusion, and post-process filters. Models derived from 3D scanning and photogrammetry were provided with textures, while those from μCT did not have associated visual data (Figure 4).

Figure 4. **3D models with an applied shader, light sources, global illumination, ambient occlusion, and post-process filters, on "Sketchfab" platform created by using different techniques**

From left to right: 3D scanning, photogrammetry, μCT

The methodology for automatically segmenting the vertebral column was validated using a cohort of 250 patient CT scans. Under the supervision of medical expert, all 25 bones of the spine (from C1 to the coccyx) were segmented and the results were verified (Figure 5).

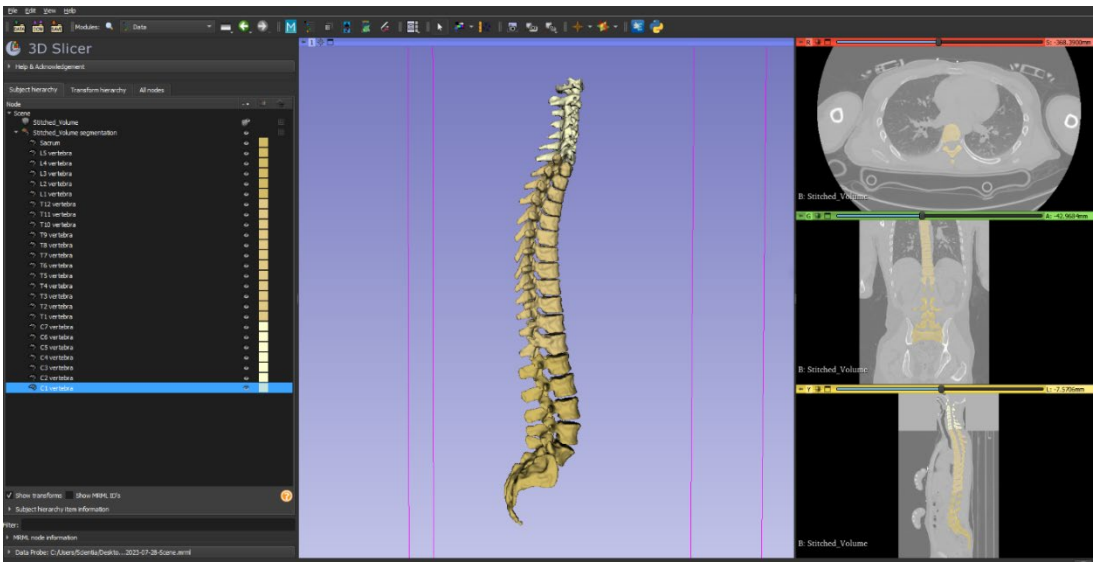

Figure 5. **Semantically segmented vertebral column serving as proof of concept of the presented methodology**

(In total, 25 bones from C1 till sacrum combined with coccyx)

The created masks were validated and corrected by comparing the segmented bones with reference anatomy from literature and software like "Complete Anatomy" (Motsinger, 2020).

Analysis of the segmentation results revealed instances of false registration anomalies (62 cases), where separate vertebrae were incorrectly identified as a single entity. Segmentation inaccuracies were also observed in all cases, where the delineated region either extended beyond or fell short of the intended anatomical boundaries, sometimes including adjacent tissues or omitting parts of the target structure (Figure 6).

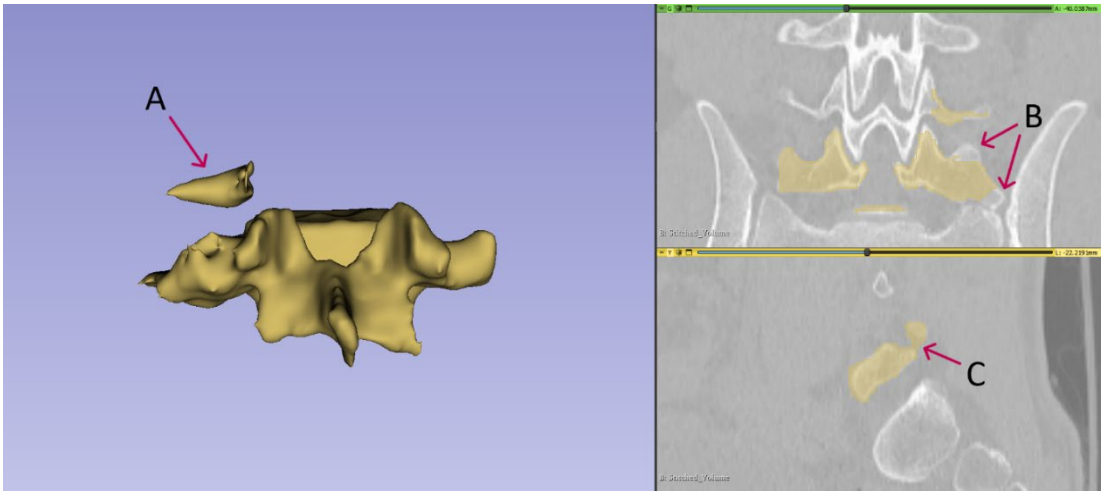

Figure 6. **Illustrative examples of artifacts in anatomical segmentation. Improper registration**

(A): A segment of the L4 vertebra is inaccurately identified as part of the L5 vertebra. Omission of critical regions (B): This artifact represents the absence of specific anatomical regions that should have been included in the segmentation. False registration (C): Soft tissues are incorrectly registered as constitutive elements of the L5 vertebra, compromising the integrity of the segmented structure.

These findings highlight the importance of rigorous validation and potential areas for improvement in automated segmentation techniques to ensure anatomical accuracy for downstream applications, including 3D printing and educational tools. The successful outcome of the automated segmentation work included the creation of a composite volume integrating cervical and thoraco-abdominal regions with corresponding segmentation masks, stored in the .NRRD file format, which offers advantages for machine learning workflows compared to the traditional DICOM format.

The integration of digital images and 3D-printed models in a Human Anatomy study course was assessed through 250 student feedback (Kazoka et al., 2021). They reported studying gross anatomy and 3D visualisations (18 % and 16 % respectively), followed by the use of 3D printed models (14 %). A small percentage (2 %) focused only on basic structures. When asked about learning from digital images and 3D printed models, students indicated a deeper understanding (19.2 %), virtual dissection (18 %), and learning about variations/abnormalities (14.8 %). Only a small number (2.8 %) mentioned the use of correct terminology (Table 3).

Table 3

Student responses to four questions in Human Anatomy study course

Question	Attitudes and Views	Students (n)	%
What did you study during the course?	Anatomical terminology	24	10
	Basic structures	5	2
	Functions of structures	25	10
	Location of structures and organs	21	8
	Topography	30	12
	Radiological anatomy	15	6
	3D visualisations of the structures	40	16
	Creation of 3D models	35	14
	Work in groups/teams	10	4
	Gross anatomy (dissection)	45	18
	More interesting learning and education	25	10
What did you study from the digital images and 3D models?	Relationships between structures	15	6
	Analysis of clinical cases	30	12
	Virtual dissection	45	18
	Different variations and/or abnormalities	37	15
	Deeper understanding of anatomy	48	19
	Simulations of clinical procedures	10	4
	Basics for clinical studies	20	8
	Overview of knowledge and skills	13	5
	Use of correct anatomical terminology	7	3
How did you solve problems or complicated situations during that time?	Including more visual aids	67	27
	Repeating material	52	21
	Help from classmates and educator	48	19
	Using more time; moving slower	32	13
	Using basic concepts	41	16
	Simplification of the information	10	4

Table 3 continued

Question	Attitudes and Views	Students (n)	%
How will the tools that you used help you in the future?	Importance of anatomy for clinical studies	65	26
	Training of some procedures	37	15
	Relationship between basic and clinical study subjects	70	28
	Basics for scientific work	13	5
	Improving clinical skills	18	7
	Success in tests/exams	47	19

Regarding problem-solving during the course, students primarily reported using more visual aids (26.8 %) and repeating material (20.8 %). Other strategies included using more time (12.8 %) and simplifying information (4 %). The tools were perceived to be helpful for future studies, particularly in understanding the relationship between basic and clinical subjects (28 %), recognising the importance of anatomy for clinical studies (26 %), and achieving success on tests and exams (18.8 %). A small group (5.2 %) related the tools to scientific work.

Overall, students expressed satisfaction with the 3D models used in the course. A significant portion (20.4 %) felt stimulated and motivated to learn more and perceived the course as more intensive due to the incorporation of digital images and 3D printed models. Students used 3D-printed models alongside digital images to study anatomy, reporting deeper understanding, opportunities for real and/or virtual dissection, and engagement with anatomical variations.

Table 4 shows the results of the students' satisfaction survey (Kazoka et al., 2021).

Table 4

Students' satisfaction using 3D models in Human Anatomy study course

Satisfaction Aspect	Students (n)	%
Reproduce taught/learned knowledge and skills	46	18
Increase motivation and intensity for learning	51	20
Develop knowledge and skills relevant to clinical needs	48	19
Improve thinking and problem-solving with respect to human-body structures	28	11
Prepare for the assessment of knowledge and skills	42	17
Provide a good background for future professional practice	35	14

Performance Evaluation of AI Models

This section outlines the experimental results derived from the application of various AI models to medical imaging datasets. The evaluation encompasses both quantitative metrics and qualitative observations, providing insights into the performance and capabilities of the developed systems in the context of image analysis.

The performance of the developed AI models was rigorously evaluated using appropriate metrics tailored to the specific tasks of segmentation in medical imaging and detection in histological slides. This subsection details the evaluation methodologies and presents the quantitative results obtained for each application area.

Performance of AI-Based Segmentation in Medical Imaging

In a study aimed at detecting and locating cancerous lesions in the spine, a U-Net model was used. The first step was to segment the entire spine, which provided the necessary context for the later analysis of the metastatic lesions. The U-Net model was trained using five-fold cross-validation and optimised with a composite loss function combining Dice loss and cross-entropy loss to enhance segmentation performance. Training was conducted on image patches extracted from the original scans, and the Dice metric was computed over these patches to assess segmentation accuracy during training. During the inference phase, a sliding window approach was utilised, which involved processing patches that might differ from those used in training, potentially leading to minor variations in the resulting Dice scores.

Validation patches were sampled using the same methodology as the training patches, ensuring consistency in the calculation of the Dice coefficient across all sampled validation data. To monitor the training progress and identify potential overfitting, a pseudo-Dice metric was employed, as depicted in Figures 7 and 8 of that study. This metric was updated iteratively throughout the training process and served as a preliminary indicator of model performance, distinct from the final Dice similarity coefficient which was computed at the conclusion of training over the entire image using a sliding window approach, providing a comprehensive evaluation of the model's accuracy on full images.

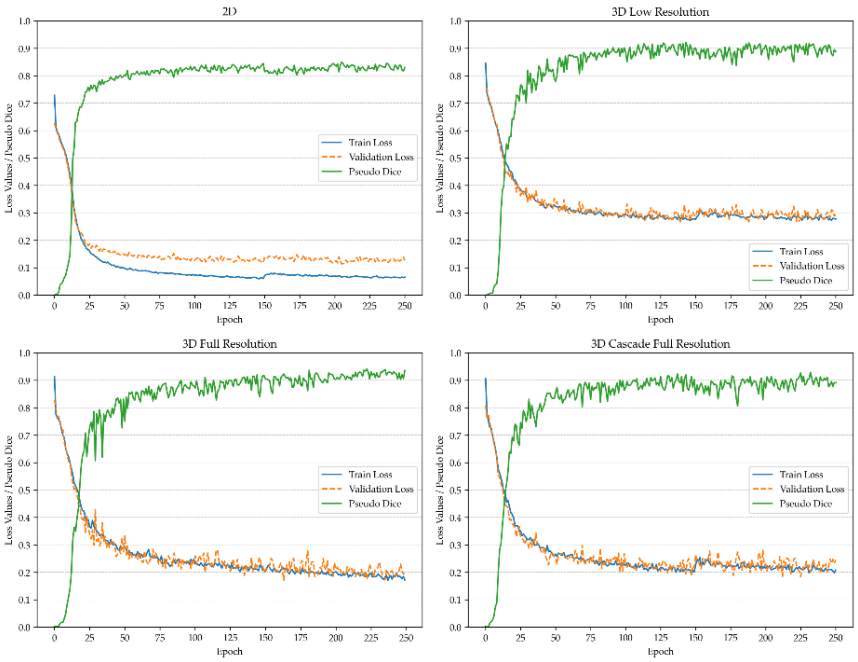

Figure 7. **Training process of the model for vertebra segmentation**

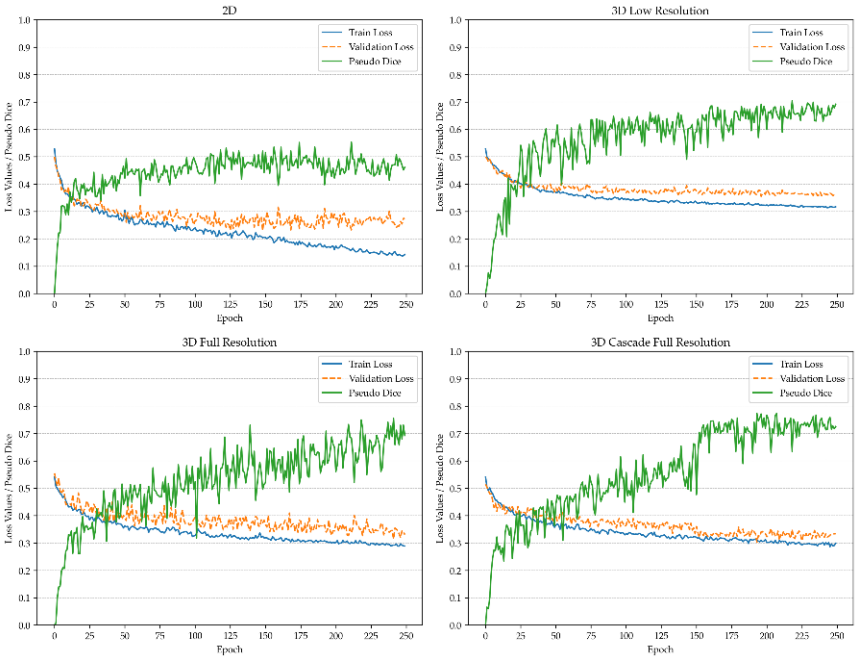

Figure 8. **Training process of the model for spinal metastasis segmentation**

Performance metrics were derived from the validation dataset using the model architecture that exhibited the highest performance during training. This structured evaluation framework facilitated a robust assessment of the U-Net model's effectiveness in both vertebra and metastasis segmentation, confirming its precision and reliability for localising and characterising metastatic regions within the vertebral column (Tables 5 and 6).

Table 5

Metrics for evaluation of "3D Cascade Full-Resolution" model for metastasis instance segmentation

Metastasis Type	Dice Similarity	F-Beta Score	Panoptic Quality
Lytic	0.71	0.68	0.45
Sclerotic	0.61	0.57	0.30

Table 6

Metrics for evaluation of "3D Full-Resolution" model for vertebrae instance segmentation

Vertebra	Dice Similarity Coefficient	F-Beta Score	Panoptic Quality
C1	0.94	0.94	0.75
C2	0.95	0.95	0.82
C3	0.93	0.93	0.75
C4	0.93	0.93	0.75
C5	0.93	0.94	0.75
C6	0.93	0.93	0.75
C7	0.94	0.93	0.79
T1	0.94	0.94	0.81
T2	0.95	0.95	0.83
T3	0.95	0.95	0.82
T4	0.95	0.95	0.83
T5	0.94	0.94	0.82
T6	0.88	0.87	0.69
T7	0.87	0.88	0.70
T8	0.91	0.92	0.75

Table 6 continued

Vertebra	Dice Similarity Coefficient	F-Beta Score	Panoptic Quality
T9	0.93	0.93	0.77
T10	0.94	0.94	0.81
T11	0.95	0.95	0.85
T12	0.95	0.94	0.84
L1	0.95	0.94	0.83
L2	0.94	0.94	0.83
L3	0.93	0.92	0.81
L4	0.94	0.89	0.84
L5	0.95	0.94	0.86
Sacrum	0.96	0.96	0.89

Figure 9 provides representative outputs from the trained 3D U-Net model for spinal metastasis segmentation. Separately, Figure 10 is dedicated to showing the masks produced by the vertebra segmentation model.

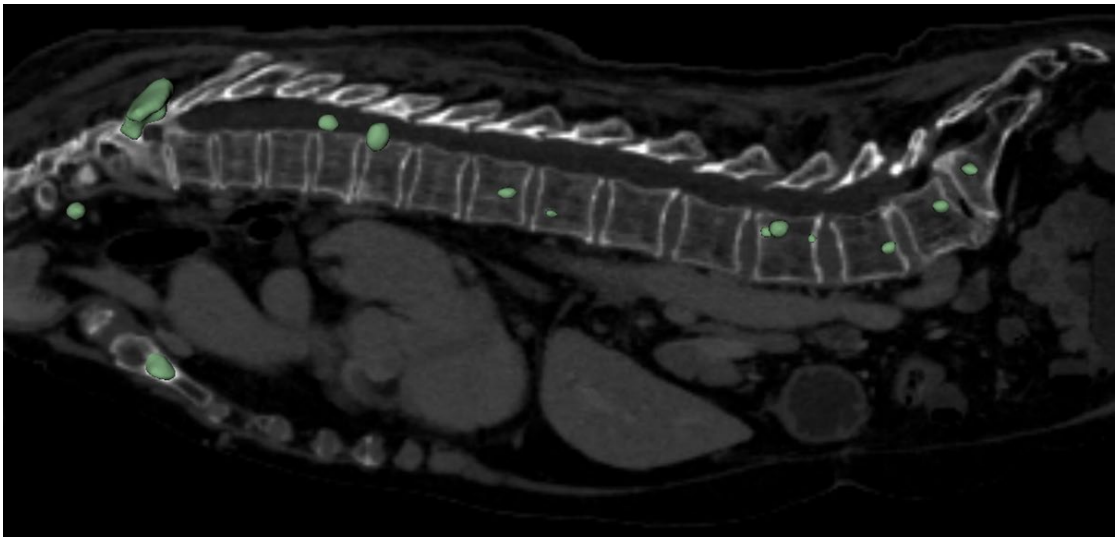

Figure 9. **Illustration of the model outputs: on the left, the predicted mask produced by the metastasis's segmentation model; on the right, the vertebra segmentation model's predicted mask with each class depicted in a distinct colour**

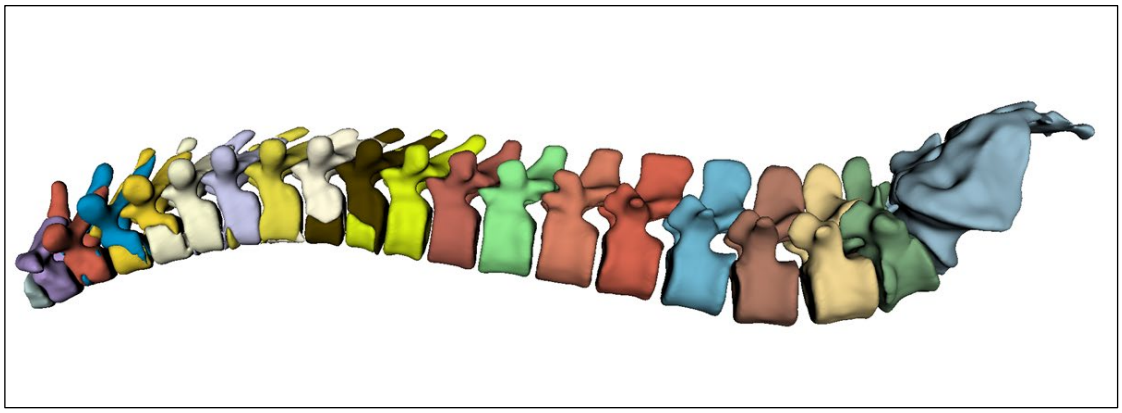

Figure 10. **Illustration of the vertebra segmentation model's predicted mask with each class depicted in a distinct colour**

Performance of AI-Based Detection in Histological Images

The primary focus of this section is on the performance of the AI models for cell detection. In the context of histological image analysis, deep neural networks were utilised for the estimation of Interstitial Cells of Cajal (ICCs) in the anal canal wall of patients with advanced haemorrhoidal disease.

Immunohistochemistry using CD117 and ANO1 was performed to identify and assess the distribution of ICCs and the membranous expression of ANO1. Immunostaining revealed ICCs as ramified cells dispersed among smooth muscle cells. The density of ICCs associated with the muscular component of the anal canal wall varied significantly among patients with haemorrhoidal disease (Figure 11). In cases with loosening of the muscular component and the presence of dilated vessels, a reduction in ICC number was observed, with cells often localised perivascularly. ANO1 immunoreactivity was primarily noted at the membrane of anal gland epithelial and smooth muscle cells, with varying expression levels across specimens.

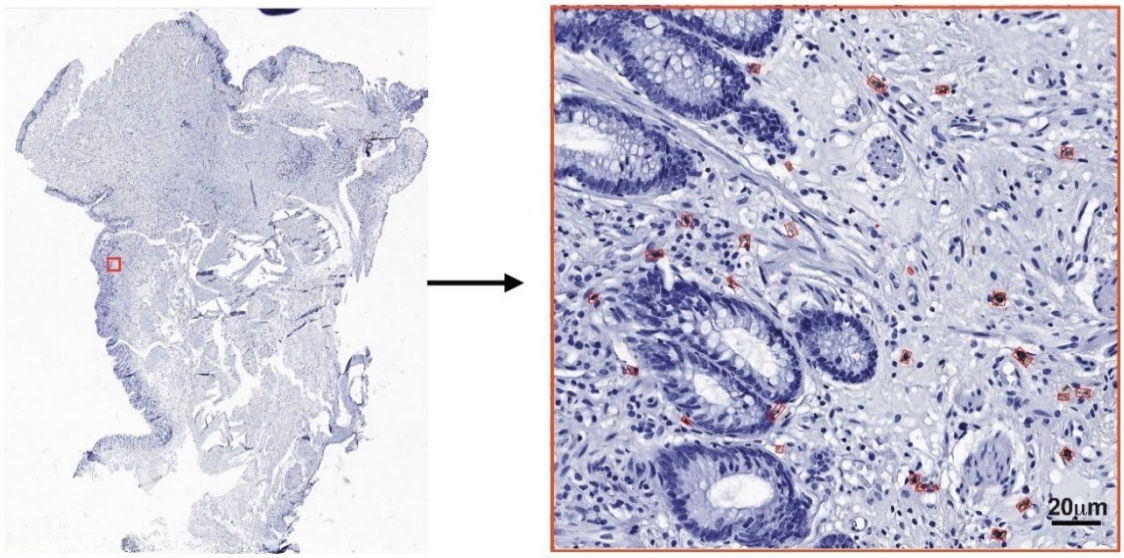

Figure 11. **Deep neural network–assisted immunohistochemical mapping of interstitial cells of Cajal in FFPE anorectal tissue**

Immunohistochemistry for ICCs was performed on formalin-fixed, paraffin-embedded anorectal specimens from haemorrhoidal disease patients. WSI were computationally segmented for regions of interest and analysed by a deep neural network to detect ICCs. Representative field showing loosening of the mucosal muscularis with irregularly oriented myocytes; brown-stained ICCs are indicated.

Several deep neural network models of different sizes were trained for ICC detection, as illustrated in Figure 12. Training was conducted over 51 epochs, and model performance was evaluated using mean Average Precision at 50 % (mAP_{50}), $mAP_{50\text{-}95}$, and F1 score. Training was halted at epoch 51, because earlier experiments that ran for up to 200 epochs showed no further performance gains beyond this point and indicated an increased risk of overfitting. All trained DNN models demonstrated comparable performance, achieving

a mAP$_{50}$ of 92 %, a recall of 86 %, and a precision of 88 %. These metrics were considered adequate for the task of cell counting. The selection of the final model for integration prioritised efficiency, balancing a low parameter count for improved performance on less powerful devices and faster inference speed. The YOLOv11n-obb model was ultimately chosen for implementation due to its optimisation for both accuracy and resource efficiency.

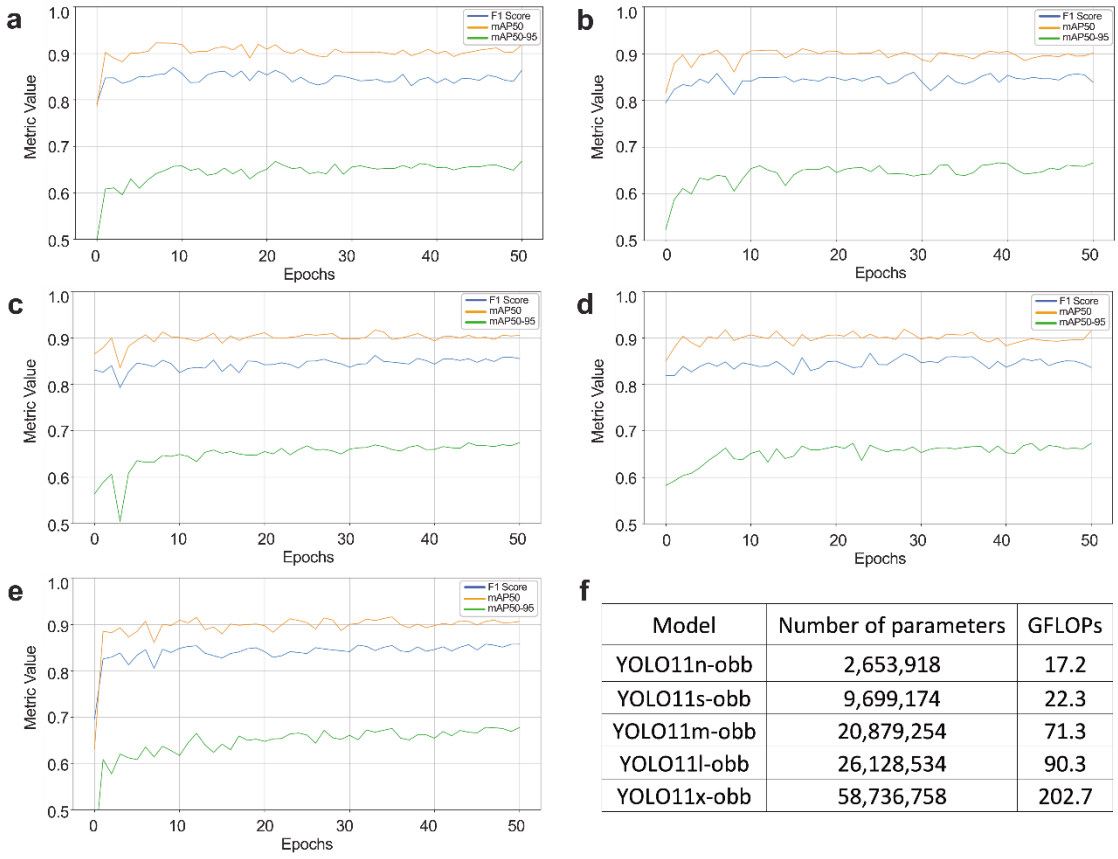

Model	Number of parameters	GFLOPs
YOLO11n-obb	2,653,918	17.2
YOLO11s-obb	9,699,174	22.3
YOLO11m-obb	20,879,254	71.3
YOLO11l-obb	26,128,534	90.3
YOLO11x-obb	58,736,758	202.7

Figure 12. **Performance of the trained models**

YOLO11n-obb (a), YOLO11s-obb (b), YOLO11m-obb (c), YOLO11l-obb (d), YOLO11x-obb (e), and parameters (f) of the trained models

A surface area quantification module was developed within the program to assess histological sections and delineate specific tissue regions. It utilises either the resolution metadata from TIFF files or a user-defined pixel size to perform pixel-to-area conversions in square millimetres. Morphological operations are applied to generate a tissue mask, enabling the computation of the tissue-occupied area relative to the entire histological slide. Following model training, the “MorpHista” (version 1.0) software was developed to efficiently process large whole slide images (WSIs) and quantify ICCs. This software integrated automated detection and post-processing steps, addressing the challenge of reassembling segmented regions after inference and consolidating detected features into a single image file with associated statistics, including ICC counts. The “MorpHista” tool (Figure 13) has been made

publicly available to facilitate reproducible ICC analysis and promote research innovation in digital pathology.

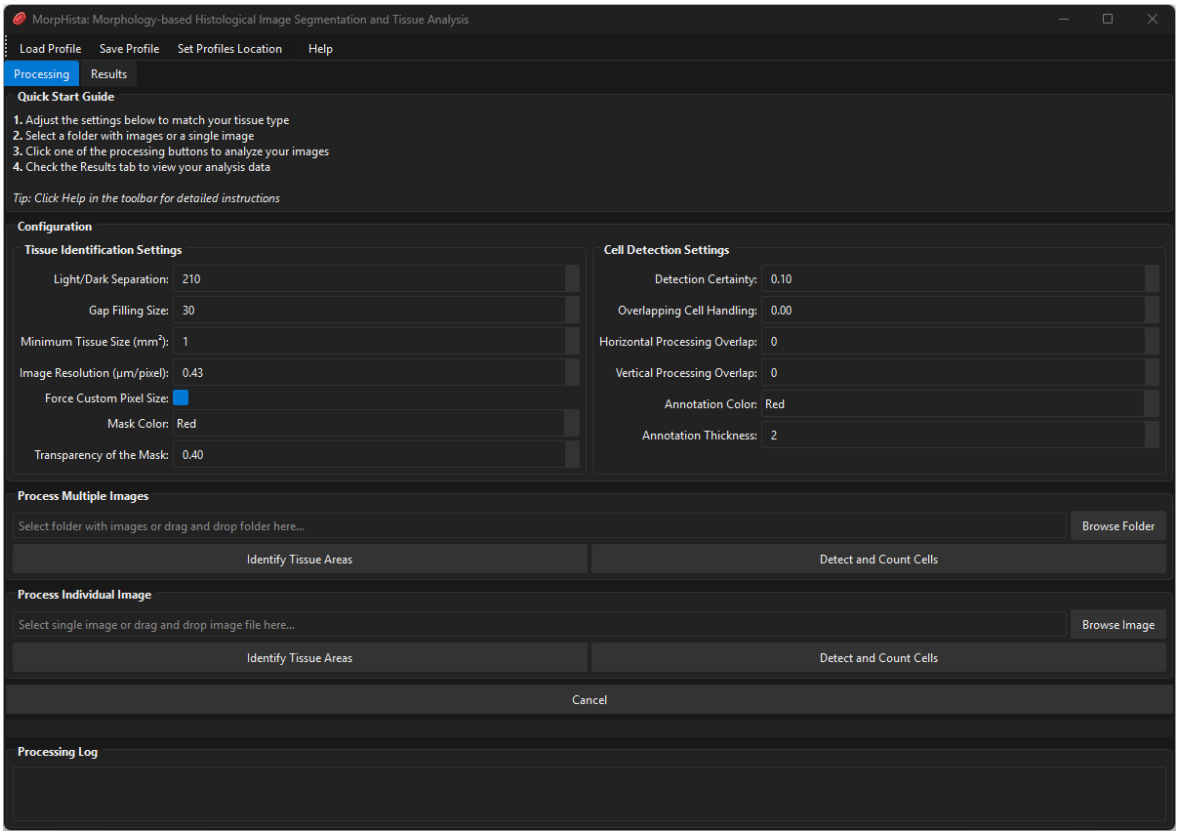

Figure 13. **User interface of "MorpHista" tool**

Building on these components, the complete MorpHista workflow operates as follows. Whole-slide immunohistochemistry images (CD117/ANO1) are imported together with resolution metadata. A tissue mask is generated by colour-based thresholding and morphological operations, enabling both exclusion of background regions and estimation of tissue area in mm². Tiles are then sampled from tissue regions and analysed by a YOLOv11n-obb detector that predicts oriented bounding boxes for interstitial cells of Cajal. Tile-level detections are mapped back to whole-slide coordinates, merged across tile borders, filtered, and intersected with the tissue mask. The final pipeline outputs per-slide ICC counts, density metrics, and visual quality-control overlays, together with machine-readable result tables for downstream statistical analysis (Figure 14).

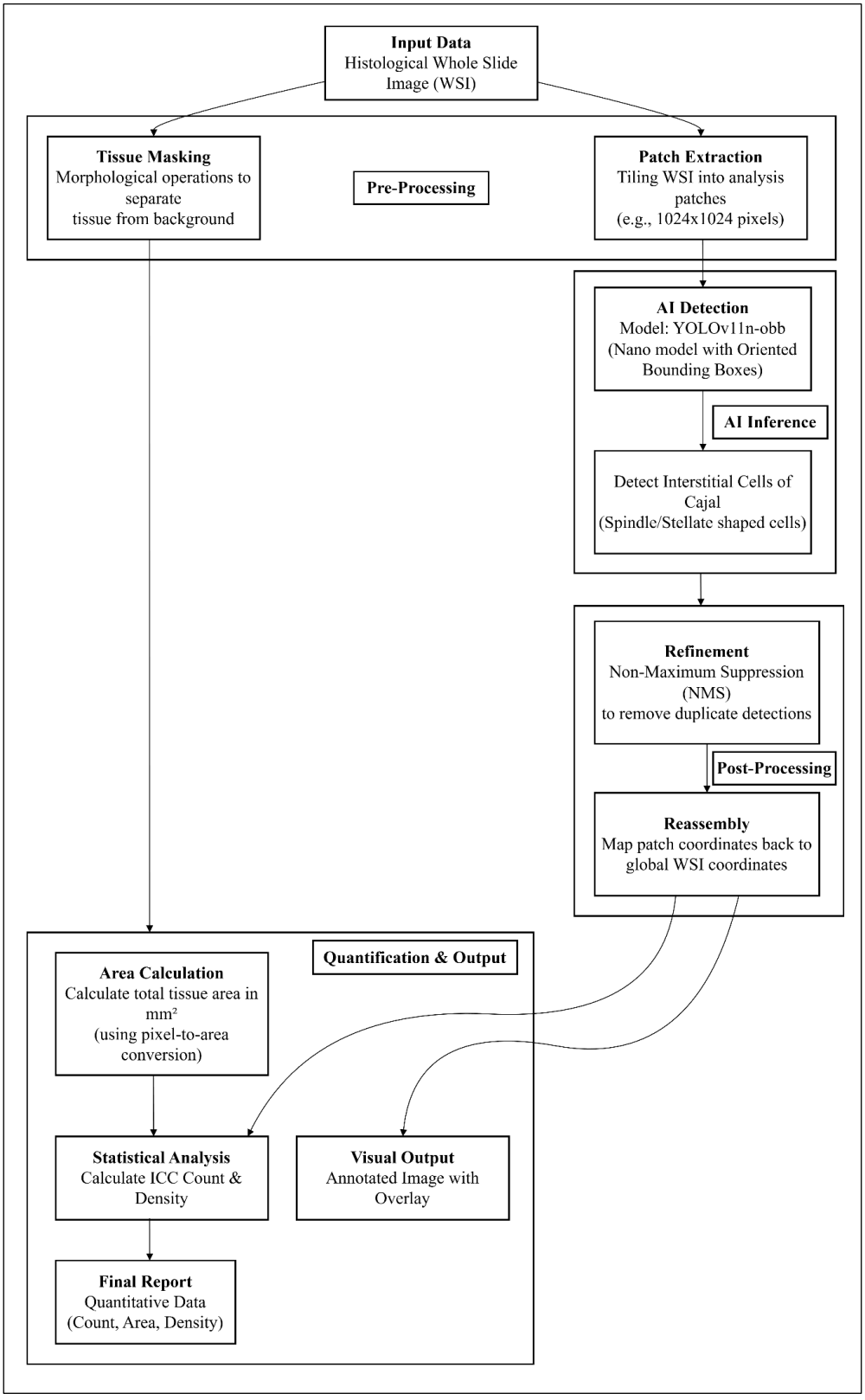

Figure 14. **Workflow of "MorpHista" software**

An attempt was made to incorporate a segmentation approach for quantifying ANO1 expression. However, the targeted Dice coefficient was not achieved. This outcome highlights the inherent complexity of pixel-level classification tasks, particularly given the variability in staining intensities and tissue morphology within the dataset. A linear regression analysis

revealed an inverse relationship between the number of ICCs and ANO1 expression in anorectal tissue from patients with advanced haemorrhoidal disease. Tissue samples exhibiting reduced ANO1 expression in myocyte membranes correlated with a higher number of ICCs, while samples with elevated ANO1 expression showed a lower number of ICCs.

To further enhance the understanding of the pathophysiology of haemorrhoidal disease, an unsupervised clustering method was applied to the research data. This analysis incorporated clinical data, immunohistochemistry data, and DNN-derived ICC quantification findings, using either five or six major factors. The clustering analysis based on six factors revealed that only 36 % of patients with Grade III haemorrhoidal disease exhibited a high density of ICCs, compared to 60 % of patients with Grade IV disease. Discomfort, pain, and bleeding were observed pre- and postoperatively in both stages. Postoperative pain was markedly reduced for both stages. A statistically significant reduction in bleeding was observed postoperatively ($p < 0.0001$). However, two patients with postoperative bleeding were diagnosed with Grade IV haemorrhoidal disease and had a high density of ICCs ($p = 0.0041$), suggesting a potential link between ICC density and disease severity.

Discussion

Interpretation of Findings: 3D Reconstruction of Morphological Structures

The integration of advanced digital technologies, particularly in the realm of 3D reconstruction of morphological structures, has profoundly impacted various fields, ranging from medical education to clinical practice and biomedical research. This section aims to provide a comprehensive analysis of the different techniques employed for 3D reconstruction, drawing upon existing literature and the specific methodologies explored in the Thesis. By examining the strengths, weaknesses, and practical considerations associated with each technique, a clearer understanding of their suitability for diverse applications can be established. Accurate segmentation and the subsequent 3D reconstruction of morphological structures form the unifying methodological axis of the Thesis, linking the 3D model-creation pipeline with the artificial intelligence workflows by providing the anatomically-grounded labels required for reconstruction, training, validation, and inference.

The creation of digital 3D models from physical specimens or imaging data can be achieved through several distinct approaches. These techniques vary in their underlying principles, required equipment, data acquisition methods, and the characteristics of the resulting 3D models.

One approach involves the use of dedicated 3D scanner. These devices capture the external geometry of an object directly, often employing technologies such as structured light, laser scanning, or photogrammetry-based systems. As demonstrated in this study (Edelmers et al., 2022), 3D scanning can capture visual data, contributing to a realistic appearance of the digital model. The choice of scanner significantly impacts the resolution and quality of the obtained texture map, with industrial-grade scanners offering higher fidelity compared to mid-level devices.

Another widely used technique is photogrammetry. This method involves taking multiple photographs of an object from different angles and using specialised software to reconstruct a 3D model based on the overlapping images. Photogrammetry is highlighted as a relatively simple and inexpensive method for creating realistic 3D digital models, capable of capturing both topological and visual data. Following specific guidelines, photogrammetry can produce metrically accurate models that are valuable for self-directed learning and understanding complex anatomical structures (Petriceks et al., 2018).

For obtaining highly detailed internal and external structural information, μCT is a powerful technique. μCT utilises X-rays to generate cross-sectional images of a specimen, which are then computationally reconstructed into a 3D volume. This method is particularly valuable for capturing the intricate inner structures of objects, such as the trabecular bone within

a bone specimen (Edelmers et al., 2022). The resulting dataset provides a high-density polygonal mesh and accurate topological data, making it suitable for applications requiring detailed structural analysis, such as implant production or biomechanical simulations.

Beyond direct scanning of physical specimens, 3D models of anatomical structures can also be generated from medical imaging data, such as CT and MRT scans (Bücking et al., 2017; Edelmers et al., 2021). These modalities provide volumetric datasets that can be processed to segment specific anatomical regions and create 3D representations. The availability of massive medical image datasets on digital platforms facilitates this approach. Differentiation of tissue density in imaging data allows for the application of segmentation techniques to isolate different anatomical structures (Van Eijnatten et al., 2018).

Increasingly, AI-driven approaches, particularly those employing machine learning and deep learning algorithms, are being integrated into the 3D reconstruction workflow, especially for the segmentation of medical images. These methods aim to automate or semi-automate the process of identifying and delineating anatomical structures within volumetric data, significantly reducing the time and effort required for manual segmentation. AI-based segmentation can be applied to a variety of anatomical structures, enhancing the efficiency of data annotation in medical imaging projects.

The application of these different techniques is often guided by the intended use of the 3D model. As categorised by this study, the main categories of implementation include visualisation, simulation, and physical replication (such as for implants or prostheses). For visualisation and educational purposes, capturing visual data and producing realistic appearances is often prioritised. For simulation and physical replication, the accuracy and density of the polygonal mesh, as well as the representation of internal structures, become more critical factors.

Methodological Challenges and Limitations in 3D Reconstruction

Despite the significant advancements in 3D reconstruction techniques, several challenges and limitations persist, impacting the accuracy, efficiency, and accessibility of this technology.

To situate the 3D reconstruction and 3D-printing protocols developed in this Thesis within the broader methodological landscape, they were compared with representative CT-based workflows described in recent reviews and implementation reports (Brumpt et al., 2023; Bücking et al., 2017; Dorweiler et al., 2021; Fedorov et al., 2012; Ferreira da-Silva et al., 2023; Flaxman et al., 2021; Leng et al., 2017). The main similarities and differences are summarised in Table 1.

Table 1

Comparison of CT-based 3D reconstruction and 3D-printing protocol developed in this Thesis with open-source workflows and commercial point-of-care 3D printing suites

Dimension	Protocols developed in this Thesis	Open-source CT→3D workflows (3D Slicer + mesh tools + slicer)	Commercial 3D modelling and printing platforms (Materialise Mimics inPrint, syngo.via)
Main purpose	Standardised CT-based bone model reconstruction and FDM printing for anatomy education and AI dataset generation	Generic patient-specific or educational models; often described as ad-hoc "how-to" case workflows	Clinical planning, device sizing, regulatory-grade models integrated in radiology workflows
Software stack	Fully open and low-cost: 3D Slicer for segmentation, MeshLab/Meshmixer for mesh editing, Cura for slicing, with explicit parameter documentation	Similar open tools (3D Slicer + mesh editor + slicer), but with more heterogeneous and less standardised parameter reporting	Proprietary integrated software (Mimics InPrint, syngo.via) with locked-in segmentation and print preparation pipelines
Segmentation & optimisation	Combines semi-automatic (and AI-assisted where applicable) segmentation with a fixed post-processing recipe tuned for FDM bone models and re-use in AI studies	Mostly thresholding, region growing and manual editing; mesh repair and smoothing described, but often without a reproducible protocol	Advanced but closed segmentation tools with presets and automated mesh optimisation for clinical use
Printing & cost	Targets affordable FDM printers, balancing anatomical fidelity and robustness; no licence costs, low per-model cost	Frequently FDM-based and low-cost, but print settings and quality assessment steps are inconsistently reported	Mix of higher-end in-house printers and external certified services; substantially higher software and implementation costs
Reproducibility & barriers	End-to-end workflow, parameters and software are fully described, facilitating replication in teaching hospitals and universities	Tools are open, but complete protocols are fragmented across reports; effective use depends on local "power users"	Highly standardised but non-transparent and expensive; adoption requires institutional budgets

A primary challenge lies in achieving and verifying the accuracy of the generated 3D models (Odeh et al., 2019; Wakjira et al., 2024). The precision of 3D printed anatomical models, for instance, is crucial for their use in education and clinical applications, but it can be influenced by the chosen printer technology. Verification of model accuracy often requires comparison with original specimens. Factors such as technical parameters, morphological variability of the specimens, and the expertise of the technical personnel can all affect the accuracy and quality of the final digital 3D models (Wendo et al., 2025).

While techniques like photogrammetry can be relatively inexpensive, high-quality 3D scanners and μCT machines represent substantial investments (Smith et al., 2018). The cost of materials and the printing process itself can also contribute to the overall expense of creating physical 3D models.

Creating a series of models through photogrammetry, for example, can be a time-consuming process (Morgan et al., 2019). Similarly, manual segmentation of anatomical structures from medical imaging data is a laborious task, although AI-driven approaches aim to mitigate this.

The process of 3D reconstruction, particularly from medical imaging, is prone to errors and artifacts. Segmentation, whether manual or semi-automated, can result in inaccuracies such as the omission of critical regions, incorrect merging of structures, and imprecise registration (Edelmers, Kazoka, et al., 2024). Pathological anomalies and anatomical variations further increase the complexity of accurate segmentation. Artifacts can also arise during the scanning process itself (Alzain et al., 2021).

The quality of the initial data is crucial as creating anatomically accurate 3D printed models requires high-resolution volumetric datasets. Low-quality input data will inevitably lead to less accurate and detailed 3D reconstructions (Edelmers et al., 2022).

Finally, the need for expert precision and validation remains crucial, even with the advent of AI-assisted methods. Manual validation of segmented structures by individuals with a high level of anatomical expertise is necessary to ensure morphological precision and methodological robustness. The lack of quantitative benchmarks for evaluating AI-segmented structures further emphasises the importance of expert oversight.

Despite these challenges, ongoing research and technological advancements continue to push the boundaries of 3D reconstruction, leading to more accurate, efficient, and accessible methods for studying and utilising morphological structures.

Interpretation of Findings: AI in Detection and Segmentation of Morphological Structures

The application of AI, particularly deep neural networks (DNNs), in the analysis of medical images for the detection and segmentation of morphological structures presents a transformative approach with significant potential to augment diagnostic capabilities. This research, building upon existing advancements in the field, demonstrates the utility of U-Net based architectures for tasks such as vertebras segmentation and the identification of spinal metastatic lesions. The capacity of these models to process complex spatial and contextual relationships within medical imaging data is crucial for accurate identification of subtle or early-stage pathological changes. The selection of the nnU-Net architecture in the study on

spinal metastatic lesions was predicated on its demonstrated versatility and robust performance across both 2D and 3D medical image data, offering an advantage over architectures like VUNet, which is primarily designed for 3D data (Hirose et al., 2019), and the more lightweight SegNet (Badrinarayanan et al., 2017), which may not achieve comparable performance in tasks requiring high-resolution predictions and detailed boundary delineation. The automatic handling of preprocessing and architecture selection by nnU-Net further contributed to its performance edge in the context of medical segmentation where accuracy is crucial.

Beyond imaging modalities, DNNs are also proving valuable in the analysis of histopathological data. The study on the estimation of Cajal cells in the anal canal wall (Fišere et al., 2025) highlights the successful integration of DNN-based models, specifically a YOLOv11-based architecture, into the pathology workflow for the precise detection and quantification of interstitial cells of Cajal (ICCs) using immunohistochemical labelling. This represents a significant step towards utilising AI for detailed histopathological analysis, moving beyond the predominant focus on clinical and imaging modalities in previous AI studies (Patel et al., 2020). The high accuracy achieved by the YOLOv11n-obb model, with a mAP_{50} of approximately 92 %, aligns with the performance of recently developed AI systems in digital pathology, underscoring the potential of DNNs for a wide range of histopathological applications (McGenity et al., 2024). Architectures such as the U-Net and its variations, including the 3D U-Net (Çiçek et al., 2016), have been particularly successful due to their encoder-decoder structure with skip connections, which allows for the effective integration of both low-level and high-level features, crucial for precise boundary delineation.

In the domain of digital pathology, object detection models like those based on the YOLO architecture are valuable for identifying and quantifying specific cellular structures within WSIs (Debsarkar et al., 2025; Wendo et al., 2025). The application of a YOLOv11-based model for the estimation of Cajal cells demonstrates the effectiveness of this approach for cell detection tasks. The model's ability to accurately identify ICCs using the CD117 marker, achieving a mAP_{50} of 92 %, indicates its potential for automating the quantification of specific cell populations in histopathological specimens. This can significantly reduce the time and effort required for manual analysis, enabling more efficient and objective assessments.

The study on spinal metastatic lesions employed different configurations of the U-Net architecture, demonstrating that the 3D full-resolution architecture achieved the highest performance for both vertebra and metastasis segmentation (Edelmers, Ņikuļins, et al., 2024). This highlights the importance of utilising architectures capable of processing the volumetric nature of imaging data when analysing structures in 3D space. The performance metrics, including the Dice similarity coefficient (DSC), F-beta score, and panoptic quality, provide

a quantitative assessment of the models' accuracy in segmenting the target structures. The results for lytic metastases, with a DSC of 0.71 and an F-beta score of 0.68, were comparable to findings in related studies utilising U-Net based models for similar tasks (Kim et al., 2024; Liu et al., 2021).

The training process for these DNN models typically involves large datasets with expert annotations. The nnU-Net framework, for instance, incorporates automated hyperparameter selection and data augmentation to optimise model performance and generalizability. Techniques such as rotations, scaling, noise injection, and variations in brightness and contrast are applied to increase the diversity of the training data and mitigate overfitting. The use of composite loss functions, combining metrics like Dice loss and cross-entropy loss, is also common to balance the accuracy of foreground-background segmentation and the precision of boundary delineation.

Methodological Challenges and Limitations in AI-Driven Medical Image Analysis

Despite the notable successes, the application of AI, particularly DNNs, in the detection and segmentation of morphological structures in medicine faces several challenges and limitations. One significant challenge is the inherent variability and complexity of medical data. Factors such as differences in imaging protocols, equipment variations, patient anatomy, and the subtle or heterogeneous appearance of pathological structures can impact model performance.

To contextualise the contribution of the "MorpHista" pipeline within current digital pathology infrastructures, it is important to compare it directly with widely used commercial and open-source platforms. Building on recent surveys of software tools and AI-enabled workflows in digital pathology (Guerrero et al., 2022; Salo et al., 2024), Table 2 summarises key dimensions, including licensing model, algorithmic transparency and customisability, supported analytical tasks, scalability to whole-slide images, hardware requirements, regulatory status, and suitability for quantitative ICC analysis. This comparison highlights how MorpHista combines the openness and extensibility typical of research-grade tools with streamlined, task-specific workflows that lower financial and technical barriers to adoption in academic and educational settings.

Table 2

Comparison of "MorpHista" software with open-source research platforms and commercial AI digital pathology systems

Dimension	MorpHista	Open-source / research platforms (QuPath, Orbit, Cytomine, ImageJ, CellProfiler, Ilastik)	Commercial AI platforms (HALO, Visiopharm, Aiforia, Paige, PathAI, Ibex, Image-Pro)
Primary focus	Automated detection and counting of interstitial cells of Cajal (ICC) in IHC whole slide images, with domain-specific metrics (surface, density) for ENS-related research	General-purpose WSI and bioimage analysis (segmentation, IHC quantification, feature extraction, machine learning) across many tissues and biomarkers	Broad portfolio of clinical and translational applications (cancer detection and grading, biomarker scoring, toxicity, clinical trials, workflow optimisation)
Task breadth	Narrow but deep: one well-defined pipeline (ICC in CD117/ANO1 slides) with tuned pre- and post-processing (tissue masking, oriented boxes, cluster handling)	Very broad: users assemble task-specific workflows (e. g. QuPath scripts, Orbit ML pipelines, Cytomine projects, ImageJ/CellProfiler macros)	Very broad: vendor-supplied and user-trainable models for many organs, stains and study types; ICC-like tasks possible but usually not pre-packaged
AI model design	Single YOLOv11n-obb detector with oriented bounding boxes for elongated spindle cells, explicitly addressing background inclusion and NMS-driven undercounting in dense clusters	Typically provide frameworks for pixel / object classifiers and sometimes DL integration, but no built-in, ICC-specific oriented detector; geometry and post-processing must be implemented by the user	Deep learning widely used (CNNs for segmentation/classification, commercial ICC-analogous tasks), but models are proprietary and optimised for mainstream clinical endpoints (e. g. prostate, breast, colorectal cancer)
Licensing and openness	Open-source research tool; full access to code, model architecture, training dataset description and evaluation metrics, enabling reproducibility and method auditing	Mostly open-source; algorithms and scripts are inspectable and modifiable, with active developer communities (especially QuPath and ImageJ)	Proprietary, closed source; internal model details and training data are generally not disclosed, although performance and some validation studies are published
User expertise required	Minimal configuration for ICC counting (input WSI + basic parameters), but assumes understanding of IHC staining and ENS morphology; retraining requires research-level expertise	Often require considerable technical knowledge (scripting, machine learning concepts, WSI infrastructure); powerful but non-trivial to configure for robust, end-to-end ICC pipelines	Front-end users' interfaces are user-friendly for pathologists, but system deployment, integration and model governance typically demand institutional IT and vendor support

Table 2 continued

Dimension	MorpHista	Open-source / research platforms (QuPath, Orbit, Cytomine, ImageJ, CellProfiler, Ilastik)	Commercial AI platforms (HALO, Visiopharm, Aiforia, Paige, PathAI, Ibex, Image-Pro)
Deployment model	Local workstation / lab server with GPU; suited for small–medium academic cohorts	Desktop or on-prem server (QuPath, Orbit, ImageJ, CellProfiler; Cytomine often server-based); more ad-hoc, research-oriented deployments	Enterprise-grade on-prem or cloud platforms, tightly integrated with scanners, hospital networks; intended for regulated clinical and pharma environments
Cost and barriers to adoption	No license cost; main barriers are hardware (GPU), WSI file handling and moderate technical setup	No or low license cost, but configuration and maintenance are labour-intensive; effective use often requires a dedicated "power user" or image analyst	Substantial licensing, maintenance and validation costs; suitable mainly for large academic centres, reference labs and industry
Fit for ICC quantification	Direct, out-of-the-box solution tuned to ICC morphology, stain characteristics and density metrics, as described in this Thesis	Technically capable but ICC pipelines must be custom-built (tiling, annotation, model training, post-processing), which is time-consuming and requires expertise	Potentially powerful but economically and organisationally disproportionate for niche research questions; ICC-specific tools are not standard offerings

In the context of spinal metastasis segmentation, the study highlighted the comparatively lower performance for sclerotic metastases compared to lytic lesions. This is attributed to the subtle imaging characteristics of sclerotic lesions, which demand higher sensitivity to subtle density changes. This underscores a limitation in current AI models to consistently detect and segment all types of lesions with equal accuracy.

Data availability and annotation remain critical bottlenecks. Training high-performing DNN models typically requires large, diverse datasets with detailed and accurate annotations. The study on spinal metastases noted that the dataset used was drawn from a single medical centre, potentially limiting the model's generalizability across different populations and imaging environments. Furthermore, the manual creation of segmentation masks by medical professionals is a time-consuming process susceptible to inter-observer variability, which can introduce inconsistencies in the training data and affect model performance and evaluation. Addressing this may require standardising segmentation protocols or employing semi-automated annotation tools.

Technical considerations, such as variability in CT scanning parameters, particularly resolution, can also significantly affect model accuracy. Discrepancies between the technical specifications of the training data and the data used for inference can reduce model

effectiveness. The relatively small dataset for metastasis detection, especially for sclerotic lesions, further impacted performance and highlighted the need for more extensive and diverse datasets to achieve higher reliability and generalizability.

Finally, the lack of validation in real-world clinical environments is a crucial limitation. Factors such as diverse patient anatomies, varying imaging conditions encountered in routine clinical practice, and workflow constraints can influence model performance. Clinical trials are essential to determine the actual impact of these AI models on diagnostic accuracy and patient outcomes in real-world settings.

Conclusions

The established aim and objectives of this doctoral research were successfully met, leading to the following conclusions:

1 A reproducible protocol was successfully developed to reconstruct 3D bone models from various medical imaging sources (including CT, μCT, photogrammetry, and 3D scanning) that emphasises systematic workflows using accessible software for data acquisition, segmentation, optimisation, and preparation for 3D printing, suitable for educational and research applications.

2 The reconstructed bone models were validated through fabrication with fused deposition modelling (3D printing) and subsequent physical and educational evaluation, which confirmed the fidelity of the digital-to-physical workflow and demonstrated the utility of the printed models in enhancing anatomical understanding in educational settings.

3 Annotated datasets were assembled for segmented morphological structures at two scales, including vertebrae with lytic and sclerotic lesions from computed tomography as well as intestinal Cajal cells from immunohistochemically stained whole-slide images, thus establishing efficient workflows to generate data suitable for AI model training and analysis.

4 Trained deep neural network models demonstrated high efficacy for the automated detection and segmentation of various morphological structures, including precise segmentation of spinal metastases from CT scans and accurate quantification of interstitial Cajal cells in histological images, confirming the hypothesis that these techniques can achieve reliable, accurate and reproducible results.

5 The developed AI methodologies were successfully integrated into functional software, exemplified by the “MorpHista” tool for automated quantification of interstitial cells of Cajal in whole-slide histological images, demonstrating practical applicability and potential to translate research findings into tools that improve efficiency in medical image analysis.

Publications and reports on topics of Doctoral Thesis

Publications:

1. **Edelmers, E.** (Corresponding Author), Kažoka, D., & Pilmane, M. Creation of Anatomically Correct and Optimized for 3D Printing Human Bones Models. Applied System Innovation, 2021, 4, 67. https://doi.org/10.3390/asi4030067, Q1.

   Author's personal technical and methodological contribution: conception and end to end implementation of a validated 3D reconstruction to printing workflow including data acquisition via photogrammetry, μCT and 3D scanning, DICOM processing, 3D Slicer segmentation, MeshLab and Meshmixer mesh optimization, Cura slicing with print validation, and technical optimization such as parameter sweeps, topology repair and decimation.

2. Kažoka, D. (Corresponding Author), Pilmane, M., & **Edelmers, E**. Facilitating Student Understanding through Incorporating Digital Images and 3D-Printed Models in a Human Anatomy Course. Education Sciences, 2021, 11, 380. https://doi.org/10.3390/educsci11080380, Q1.

   Author's personal technical and methodological contribution: design, fabrication, and validation of the 3D models used in the teaching intervention.

3. **Edelmers, E.** (Corresponding Author), Kazoka, D., Bolocko, K., Pilmane, M. Different Techniques of Creating Bone Digital 3D Models from Natural Specimens. Applied System Innovation, 2022, 5, 85. https://doi.org/10.3390/asi5040085, Q1.

   Author's personal technical and methodological contribution: development of comparative pipelines for 3D scanning, photogrammetry and μCT, implementation of complete software workflows including image and volume import, segmentation, meshing, optimization and texture handling, and comprehensive dataset preparation.

4. **Edelmers, E.** (Corresponding Author), Kazoka, D., Bolocko, K., Sudars, K., Pilmane, M. Automatization of CT Annotation: Combining AI Efficiency with Expert Precision. Diagnostics, 2024, 14, 185. https://doi.org/10.3390/diagnostics14020185, Q1.

   Author's personal technical and methodological contribution: design of the AI assisted CT annotation pipeline including dataset assembly and curation, preprocessing and series stitching, U Net configuration, semi-automatic mask generation with expert refinement, and quality control with anatomical validation.

5. **Edelmers, E.** (Corresponding Author), Nikulins, A., Sprudža, K. L., Stapulone, P., Saimons Pūce, N., Skrebele, E., Siņicina, E. E., Cīrule, V., Kazuša, A., & Boločko, K. AI-Assisted Detection and Localization of Spinal Metastatic Lesions. Diagnostics, 2024, 14, 2458. https://doi.org/10.3390/diagnostics14212458, Q1.

   Author's personal technical and methodological contribution: study design and data annotation, curation of vertebrae and metastasis datasets, training and evaluation of U-Net models for vertebral segmentation and metastasis instance segmentation, and specification of evaluation metrics.

6. Fišere, I., **Edelmers, E.** (Corresponding Author), Svirskis, Š., & Groma, V. (Corresponding Author). (2025). Utilisation of Deep Neural Networks for Estimation of Cajal Cells in the Anal Canal Wall of Patients with Advanced Haemorrhoidal Disease Treated by LigaSure Surgery. Cells, 14(7), 550. https://doi.org/10.3390/cells14070550, Q1.

   Author's personal technical and methodological contribution: development of the computational pipeline and software for ICC detection and quantification, including WSI patch extraction, data annotation, object detection with YOLOv11n-obb model, training and validation protocols with metric computation, and the creation of the "MorpHista" tool for whole slide post processing.

Reports and theses at international congresses and conferences:

1. **Edelmers, E.** (2023). Digitalization of Zygomatic Bone as a Part of the Orbit Wall. In P. Fedirko, M. Pilmane, O. Maksymuk, T. F. Babenko, & N. A. Garkava (Eds.), Practical Ophthalmology. Medical and Environmental Problems of our Days: Collection of Works International Scientific and Practical Interdisciplinary Conference (pp. 36-38). State Institution «National Research Center for Radiation medicine of the National Academy of Medical Sciences of Ukraine". https://science.rsu.lv/ws/portalfiles/portal/63211535/Digitalization_of_zygomatic_bone.pdf
2. Sudars, K., Namatevs, I., Nikulins, A., **Edelmers, E.**, Neimane, L., Slaidiņa, A., & Radziņš, O. (2023). Artificial Intelligence-Powered System for Identifying Bone Deterioration in Radiological Imaging. Paper presented at International Workshop on Embedded Digital Intelligence (iWoEDI"2023), Riga, Latvia. https://events.edi.lv/iwoedi2023/wp-content/uploads/sites/2/2023/06/IWoEDI-2023-Artificial-Inteligence-Powered-System-for-Identifying-Bone-Deterioration-in-Radiological-Imaging.pdf
3. **Edelmers, E.** (2024). 3D Gaussian Splatting for Real-Time Radiance Field Rendering in Anatomy Education and 3D Model Creation. 26. Abstract from 11th Baltic Morphology Meeting, Rīga, Latvia. https://doi.org/10.25143/rsu-balt-morf-11-meeting
4. **Edelmers, E.**, & Fišere, I. (2024). Deep Learning-Based Software for Automated Cell Detection and Counting in Whole-Slide Histological Image Analysis. 67. Abstract from 11th Baltic Morphology Meeting, Rīga, Latvia. https://doi.org/10.25143/rsu-balt-morf-11-meeting
5. **Edelmers, E.**, & Kažoka, D. (2021). Creation of digital bones collection with anatomically correct and optimized 3D models. 540. Abstract from RSU Research week 2021: Knowledge for Use in Practice, Rīga, Latvia.
6. **Edelmers, E.**, Kažoka, D., & Šmite, K. (2025). Automatic Segmentation of Morphological Structures, Metastasis Detection, and 3D Model Reconstruction from Medical Imaging Utilising Artificial Intelligence Based on Deep Neural Network Methodologies. 104. Abstract from Rīga Stradiņš University International Research Conference on Medical and Health Care Sciences "Knowledge for Use in Practice", Riga, Latvia. https://doi.org/10.25143/rw2025.kup.abstracts-book

References

1. Alzain, A. F., Elhussein, N., Fadulelmulla, I. A., Ahmed, A. M., Elbashir, M. E., & Elamin, B. A. (2021). Common computed tomography artifact: Source and avoidance. *Egyptian Journal of Radiology and Nuclear Medicine*, *52*(1), 151. https://doi.org/10.1186/s43055-021-00530-0

2. Badrinarayanan, V., Kendall, A., & Cipolla, R. (2017). SegNet: A Deep Convolutional Encoder-Decoder Architecture for Image Segmentation. *IEEE Transactions on Pattern Analysis and Machine Intelligence*, *39*(12), 2481–2495. https://doi.org/10.1109/TPAMI.2016.2644615

3. Bankhead, P., Loughrey, M. B., Fernández, J. A., Dombrowski, Y., McArt, D. G., Dunne, P. D., McQuaid, S., Gray, R. T., Murray, L. J., Coleman, H. G., James, J. A., Salto-Tellez, M., & Hamilton, P. W. (2017). QuPath: Open source software for digital pathology image analysis. *Scientific Reports*, *7*(1), Article 1. https://doi.org/10.1038/s41598-017-17204-5

4. Bidgood, W. D., Horii, S. C., Prior, F. W., & Van Syckle, D. E. (1997). Understanding and Using DICOM, the Data Interchange Standard for Biomedical Imaging. *Journal of the American Medical Informatics Association*, *4*(3), 199–212. https://doi.org/10.1136/jamia.1997.0040199

5. Boykov, Y. Y., & Jolly, M.-P. (2001). Interactive graph cuts for optimal boundary & region segmentation of objects in N-D images. *Proceedings Eighth IEEE International Conference on Computer Vision. ICCV 2001*, *1*, 105–112. https://doi.org/10.1109/ICCV.2001.937505

6. Brumpt, E., Bertin, E., Tatu, L., & Louvrier, A. (2023). 3D printing as a pedagogical tool for teaching normal human anatomy: A systematic review. *BMC Medical Education*, *23*(1), Article 1. https://doi.org/10.1186/s12909-023-04744-w

7. Bücking, T. M., Hill, E. R., Robertson, J. L., Maneas, E., Plumb, A. A., & Nikitichev, D. I. (2017). From medical imaging data to 3D printed anatomical models. *PLOS ONE*, *12*(5), e0178540. https://doi.org/10.1371/journal.pone.0178540

8. Çiçek, Ö., Abdulkadir, A., Lienkamp, S. S., Brox, T., & Ronneberger, O. (2016). 3D U-Net: Learning Dense Volumetric Segmentation from Sparse Annotation. In S. Ourselin, L. Joskowicz, M. R. Sabuncu, G. Unal, & W. Wells (Eds), *Medical Image Computing and Computer-Assisted Intervention – MICCAI 2016* (Vol. 9901, pp. 424–432). Springer International Publishing. https://doi.org/10.1007/978-3-319-46723-8_49

9. Cignoni, P., Callieri, M., Corsini, M., Dellepiane, M., Ganovelli, F., & Ranzuglia, G. (2008). MeshLab: An Open-Source Mesh Processing Tool. In *Eurographics Italian Chapter Conference* (p. 8 pages). The Eurographics Association. https://doi.org/10.2312/LOCALCHAPTEREVENTS/ITALCHAP/ITALIANCHAPCONF2008/129-136

10. Debsarkar, S. S., Aronow, B., & Prasath, V. B. S. (2025). Advancements in automated nuclei segmentation for histopathology using you only look once-driven approaches: A systematic review. *Computers in Biology and Medicine*, *190*, 110072. https://doi.org/10.1016/j.compbiomed.2025.110072

11. Dorweiler, B., Baqué, P. E., Chaban, R., Ghazy, A., & Salem, O. (2021). Quality Control in 3D Printing: Accuracy Analysis of 3D-Printed Models of Patient-Specific Anatomy. *Materials*, *14*(4), 1021. https://doi.org/10.3390/ma14041021

12. Edelmers, E. (2024). *CT Scans of Spine with Metastases (Lytic, Sclerotic)* [Data set]. Zenodo. https://doi.org/10.5281/ZENODO.13645870

13. Edelmers, E. (2025). *Segmented ICC Dataset in IHC-Stained Haemorrhoidal Disease Specimens* [Data set]. Zenodo. https://doi.org/10.5281/ZENODO.14900510

14. Edelmers, E., Kazoka, D., Bolocko, K., & Pilmane, M. (2022). Different Techniques of Creating Bone Digital 3D Models from Natural Specimens. *Applied System Innovation*, *5*(4), 85. https://doi.org/10.3390/asi5040085

15. Edelmers, E., Kazoka, D., Bolocko, K., Sudars, K., & Pilmane, M. (2024). Automatization of CT Annotation: Combining AI Efficiency with Expert Precision. *Diagnostics*, *14*(2), 185. https://doi.org/10.3390/diagnostics14020185

16. Edelmers, E., Kazoka, D., & Pilmane, M. (2021). Creation of Anatomically Correct and Optimized for 3D Printing Human Bones Models. *Applied System Innovation*, *4*(3), 67. https://doi.org/10.3390/asi4030067

17. Edelmers, E., Ņikuļins, A., Sprūdža, K. L., Stapulone, P., Pūce, N. S., Skrebele, E., Siņicina, E. E., Cīrule, V., Kazuša, A., & Boločko, K. (2024). AI-Assisted Detection and Localization of Spinal Metastatic Lesions. *Diagnostics*, *14*(21), Article 21. https://doi.org/10.3390/diagnostics14212458

18. Edgar, H., Daneshvari Berry, S., Moes, E., Adolphi, N., Bridges, P., & Nolte, K. (n.d.). *New Mexico Decedent Image Database (NMDID)*. University of New Mexico. https://doi.org/10.25827/5S8C-N515

19. Escobar Díaz Guerrero, R., Carvalho, L., Bocklitz, T., Popp, J., & Oliveira, J. L. (2022). Software tools and platforms in Digital Pathology: A review for clinicians and computer scientists. *Journal of Pathology Informatics*, *13*, 100103. https://doi.org/10.1016/j.jpi.2022.100103

20. Fedorov, A., Beichel, R., Kalpathy-Cramer, J., Finet, J., Fillion-Robin, J.-C., Pujol, S., Bauer, C., Jennings, D., Fennessy, F., Sonka, M., Buatti, J., Aylward, S., Miller, J. V., Pieper, S., & Kikinis, R. (2012). 3D Slicer as an image computing platform for the Quantitative Imaging Network. *Magnetic Resonance Imaging*, *30*(9), Article 9. https://doi.org/10.1016/j.mri.2012.05.001

21. Ferreira da-Silva, A., Donato, M. C., Oliveira da-Silva, M., Gonçalves de-Sousa, S. D., Parada Simão, T. R., Simone Kietzer, K., Liberti, E. A., & Frank, P. W. (2023). Prototyping and 3D Printing of Computed Tomography Images with an Emphasis on Soft Tissues, Especially Muscles, for Teaching Human Anatomy. *International Journal of Morphology*, *41*(1), 73–78. https://doi.org/10.4067/S0717-95022023000100073

22. Fišere, I., Edelmers, E., Svirskis, Š., & Groma, V. (2025). Utilisation of Deep Neural Networks for Estimation of Cajal Cells in the Anal Canal Wall of Patients with Advanced Haemorrhoidal Disease Treated by LigaSure Surgery. *Cells*, *14*(7), 550. https://doi.org/10.3390/cells14070550

23. Flaxman, T. E., Cooke, C. M., Miguel, O. X., Sheikh, A. M., & Singh, S. S. (2021). A review and guide to creating patient specific 3D printed anatomical models from MRI for benign gynecologic surgery. *3D Printing in Medicine*, *7*(1), 17. https://doi.org/10.1186/s41205-021-00107-7

24. Grady, L. (2006). Random Walks for Image Segmentation. *IEEE Transactions on Pattern Analysis and Machine Intelligence*, *28*(11), 1768–1783. https://doi.org/10.1109/TPAMI.2006.233

25. Ha, J. Y., Jeon, K. N., Bae, K., & Choi, B. H. (2017). Effect of Bone Reading CT software on radiologist performance in detecting bone metastases from breast cancer. *The British Journal of Radiology*, *90*(1072), 20160809. https://doi.org/10.1259/bjr.20160809

26. Hammon, M., Dankerl, P., Tsymbal, A., Wels, M., Kelm, M., May, M., Suehling, M., Uder, M., & Cavallaro, A. (2013). Automatic detection of lytic and blastic thoracolumbar spine metastases on computed tomography. *European Radiology*, *23*(7), 1862–1870. https://doi.org/10.1007/s00330-013-2774-5

27. Hirose, N., Sadeghian, A., Xia, F., Martin-Martin, R., & Savarese, S. (2019). VUNet: Dynamic Scene View Synthesis for Traversability Estimation Using an RGB Camera. *IEEE Robotics and Automation Letters*, *4*(2), 2062–2069. https://doi.org/10.1109/LRA.2019.2894869

28. Isensee, F., Jaeger, P. F., Kohl, S. A. A., Petersen, J., & Maier-Hein, K. H. (2021). nnU-Net: A self-configuring method for deep learning-based biomedical image segmentation. *Nature Methods*, *18*(2), 203–211. https://doi.org/10.1038/s41592-020-01008-z

29. Kavvadia, E.-M., Katsoula, I., Angelis, S., & Filippou, D. (2023). The Anatomage Table: A Promising Alternative in Anatomy Education. *Cureus*. https://doi.org/10.7759/cureus.43047

30. Kazoka, D., Pilmane, M., & Edelmers, E. (2021). Facilitating Student Understanding through Incorporating Digital Images and 3D-Printed Models in a Human Anatomy Course. *Education Sciences*, *11*(8), Article 8. https://doi.org/10.3390/educsci11080380

31. Khanam, R., & Hussain, M. (2024). *YOLOv11: An Overview of the Key Architectural Enhancements* (Version 1). arXiv. https://doi.org/10.48550/ARXIV.2410.17725

32. Kikinis, R., Pieper, S. D., & Vosburgh, K. G. (2014). 3D Slicer: A Platform for Subject-Specific Image Analysis, Visualization, and Clinical Support. In F. A. Jolesz (Ed.), *Intraoperative Imaging and Image-Guided Therapy* (pp. 277–289). Springer New York. https://doi.org/10.1007/978-1-4614-7657-3_19

33. Kim, D. H., Seo, J., Lee, J. H., Jeon, E.-T., Jeong, D., Chae, H. D., Lee, E., Kang, J. H., Choi, Y.-H., Kim, H. J., & Chai, J. W. (2024). Automated Detection and Segmentation of Bone Metastases on Spine MRI Using U-Net: A Multicenter Study. *Korean Journal of Radiology*, *25*(4), 363. https://doi.org/10.3348/kjr.2023.0671

34. Leng, S., McGee, K., Morris, J., Alexander, A., Kuhlmann, J., Vrieze, T., McCollough, C. H., & Matsumoto, J. (2017). Anatomic modeling using 3D printing: Quality assurance and optimization. *3D Printing in Medicine*, *3*(1), 6. https://doi.org/10.1186/s41205-017-0014-3

35. Litjens, G., Kooi, T., Bejnordi, B. E., Setio, A. A. A., Ciompi, F., Ghafoorian, M., Van Der Laak, J. A. W. M., Van Ginneken, B., & Sánchez, C. I. (2017). A survey on deep learning in medical image analysis. *Medical Image Analysis*, *42*, 60–88. https://doi.org/10.1016/j.media.2017.07.005

36. Liu, P., Lu, L., Zhang, J., Huo, T., Liu, S., & Ye, Z. (2021). Application of Artificial Intelligence in Medicine: An Overview. *Current Medical Science*, *41*(6), 1105–1115. https://doi.org/10.1007/s11596-021-2474-3

37. Ma, J., Shao, W., Ye, H., Wang, L., Wang, H., Zheng, Y., & Xue, X. (2018). Arbitrary-Oriented Scene Text Detection via Rotation Proposals. *IEEE Transactions on Multimedia*, *20*(11), 3111–3122. https://doi.org/10.1109/TMM.2018.2818020

38. McGenity, C., Clarke, E. L., Jennings, C., Matthews, G., Cartlidge, C., Freduah-Agyemang, H., Stocken, D. D., & Treanor, D. (2024). Artificial intelligence in digital pathology: A systematic review and meta-analysis of diagnostic test accuracy. *Npj Digital Medicine*, *7*(1), 114. https://doi.org/10.1038/s41746-024-01106-8

39. Milletari, F., Navab, N., & Ahmadi, S.-A. (2016). V-Net: Fully Convolutional Neural Networks for Volumetric Medical Image Segmentation. *2016 Fourth International Conference on 3D Vision (3DV)*, 565–571. https://doi.org/10.1109/3DV.2016.79

40. Morgan, B., Ford, A. L. J., & Smith, M. J. (2019). Standard methods for creating digital skeletal models using structure-from-motion photogrammetry. *American Journal of Physical Anthropology*, *169*(1), 152–160. https://doi.org/10.1002/ajpa.23803

41. Motsinger, S. K. (2020). Complete Anatomy. *Journal of the Medical Library Association*, *108*(1). https://doi.org/10.5195/jmla.2020.853

42. Neubeck, A., & Van Gool, L. (2006). Efficient Non-Maximum Suppression. *18th International Conference on Pattern Recognition (ICPR'06)*, 850–855. https://doi.org/10.1109/ICPR.2006.479

43. Odeh, M., Levin, D., Inziello, J., Lobo Fenoglietto, F., Mathur, M., Hermsen, J., Stubbs, J., & Ripley, B. (2019). Methods for verification of 3D printed anatomic model accuracy using cardiac models as an example. *3D Printing in Medicine*, *5*(1), Article 1. https://doi.org/10.1186/s41205-019-0043-1

44. Patel, V., Khan, M. N., Shrivastava, A., Sadiq, K., Ali, S. A., Moore, S. R., Brown, D. E., & Syed, S. (2020). Artificial Intelligence Applied to Gastrointestinal Diagnostics: A Review. *Journal of Pediatric Gastroenterology and Nutrition*, *70*(1), 4–11. https://doi.org/10.1097/MPG.0000000000002507

45. Petriceks, A. H., Peterson, A. S., Angeles, M., Brown, W. P., & Srivastava, S. (2018). Photogrammetry of Human Specimens: An Innovation in Anatomy Education. *Journal of Medical Education and Curricular Development*, *5*, 2382120518799356. https://doi.org/10.1177/2382120518799356

46. Ronneberger, O., Fischer, P., & Brox, T. (2015). *U-Net: Convolutional Networks for Biomedical Image Segmentation* (Version 1). arXiv. https://doi.org/10.48550/ARXIV.1505.04597

47. Salo, I., Nordlund, L., Eklund, L., Ho, J., Soini, M., Kumar, D., Yeong, J., Guan, F., & Metsälä, E. (2024). Advancements and applications of AI technologies in pathology: A scoping review. *Computer Methods in Biomechanics and Biomedical Engineering: Imaging & Visualization*, *12*(1), 2396595. https://doi.org/10.1080/21681163.2024.2396595

48. Smith, C. F., Tollemache, N., Covill, D., & Johnston, M. (2018). Take away body parts! An investigation into the use of 3D-printed anatomical models in undergraduate anatomy education. *Anatomical Sciences Education*, *11*(1), 44–53. https://doi.org/10.1002/ase.1718

49. Stritt, M., Stalder, A. K., & Vezzali, E. (2020). Orbit Image Analysis: An open-source whole slide image analysis tool. *PLOS Computational Biology*, *16*(2), e1007313. https://doi.org/10.1371/journal.pcbi.1007313

50. Van Eijnatten, M., Van Dijk, R., Dobbe, J., Streekstra, G., Koivisto, J., & Wolff, J. (2018). CT image segmentation methods for bone used in medical additive manufacturing. *Medical Engineering & Physics*, *51*, 6–16. https://doi.org/10.1016/j.medengphy.2017.10.008

51. Wakjira, Y., Kurukkal, N. S., & Lemu, H. G. (2024). Assessment of the accuracy of 3D printed medical models through reverse engineering. *Heliyon*, *10*(11), e31829. https://doi.org/10.1016/j.heliyon.2024.e31829

52. Wasserthal, J., Breit, H.-C., Meyer, M. T., Pradella, M., Hinck, D., Sauter, A. W., Heye, T., Boll, D., Cyriac, J., Yang, S., Bach, M., & Segeroth, M. (2023). TotalSegmentator: Robust Segmentation of 104 Anatomic Structures in CT Images. *Radiology: Artificial Intelligence*, e230024. https://doi.org/10.1148/ryai.230024

53. Wendo, K., Behets, C., Barbier, O., Herman, B., Schubert, T., Raucent, B., & Olszewski, R. (2025). Dimensional Accuracy Assessment of Medical Anatomical Models Produced by Hospital-Based Fused Deposition Modeling 3D Printer. *Journal of Imaging*, *11*(2), 39. https://doi.org/10.3390/jimaging11020039

54. Yushkevich, P. A., Piven, J., Hazlett, H. C., Smith, R. G., Ho, S., Gee, J. C., & Gerig, G. (2006). User-guided 3D active contour segmentation of anatomical structures: Significantly improved efficiency and reliability. *NeuroImage*, *31*(3), 1116–1128. https://doi.org/10.1016/j.neuroimage.2006.01.015